DOCTORAL THESIS

Analysis of Neuroelectromagnetic Problems via Subspace Decomposition Imaging and Inverse Algorithm

BY

Feng Luan

August 2012

DEPARTMENT OF ELECTRICAL ENGINEERING AND
COMPUTER SCIENCE
COLLEGE OF ENGINEERING
SEOUL NATIONAL UNIVERSITY

공학박사학위 논문

Analysis of Neuroelectromagnetic Problems via Subspace Decomposition Imaging and Inverse Algorithm

부분공간분해영상법 및 역알고리즘을 이용한
신경전자기 문제 해석

2012 년 8 월

서울대학교 대학원
전기 컴퓨터 공학부
루 안 펑

Abstract

Feng Luan
School of Electrical Engineering and Computer Science
The Graduate School
Seoul National University

Magnetoencephalography (MEG) is a common noninvasive biomedical technique used to measure weak electromagnetic fields generated by some ensembles of neurons inside the brain with high temporal resolution. The main objective of neuroelectromagnetic source signal analysis is to accurately estimate the location, distribution of a neuronal signal at a fine time series resolution, and to provide functional information about source dynamics based on the outside electromagnetic field measurement. Since the widely recognized ill-posed problem of the neuroelectromagnetic source imaging, the source signal estimation is not unique unless some possible and reasonable constraints are imposed, and consequently various methods have been proposed in this thesis to obtain an optimal resolution by adding computationally tractable and biophysically plausible constraints to the source imaging algorithms.

The abilities of the generalized cross validation (GCV) method and the L-curve method for the determination of the optimal regularization parameter are studied and compared for the inverse algorithms of neuroelectromagnetic problems. The results verify that the GCV method is a better choice when the measurement noise is relatively high, and the L-curve method seems to be

more effective when the source is mainly dominated by errors such as brain perturbation.

An improved inverse algorithm for precisely estimating the correlated neuroelectromagnetic activities in the deep source space is proposed. A novel weighting matrix building method obtained from the sensitivity similarity degree of the sensor array between the sources is presented, so as to enhance the property representation for the correlated deep sources. The results confirm that the proposed technique provides more detailed information for the source estimation, improves the result accuracy, and is physically more reasonable than the conventional inverse algorithms.

Recent studies on neuroelectromagnetic inverse problems have shown that a satisfactory understanding of source mechanisms requires to perform source connectivity analysis. This thesis studies inverse algorithms for reconstructing the source connectivity network. The results confirm that the noise effect for linear estimation algorithm is direct, while, for spatial filtering technique the effect is indirect. Linear estimation is advantageous for the connectivity reconstruction of high quality outside electromagnetic measurements, while, the benefit for the case of spatial filter is the low measurement environments. This thesis also proposes a modified spatial filtering algorithm to improve the source connectivity reconstruction by using the correlation gram matrix. The results show that the proposed algorithm can increase the reconstruction accuracy, decrease the error fluctuation and enhance the representation for profiles of the original source connectivity network.

Finally, this thesis proposes a subspace decomposition imaging (SDI) method for measuring a neuroelectromagnetic source signal. The SDI technique is based on spatiotemporal signal analysis from a matrix perspective that decomposes the source into low-rank and sparse components in a manner consistent with the underlying bio-mechanism in statistics. The SDI method can capture dynamic details in the source space that would sometimes be too weak to be recognized by conventional methods, but can also recover the stationary source signal contaminated by large brain perturbation. The results establish the feasibility of the SDI method for neuroelectromagnetic source signal measurement, with resulting solutions that provide substantial performance improvement over conventional methods. Moreover, noise suppression in MEG measurement is particularly challenging because it is difficult to remove the noise and preserve the information components in the MEG data. In this thesis, a novel noise suppression method, based on SDI technique, is also studied and applied to neuroelectromagnetic source estimation. The results show that the proposed method can significantly improve the estimation performance.

Keywords: Electromagnetic brain imaging, magnetoencephalography (MEG), neuroelectromagnetic inverse problem, source signal imaging, subspace decomposition imaging (SDI)

Student Number: 2008-31105

Table of Contents

Abstract ..... **i**
Table of Contents ..... **iv**
List of Figures ..... **vi**
List of Tables ..... **ix**
1 Introduction **1**
2 Regularization Techniques for Neuroelectromagnetic Source Imaging **8**
2.1 Introduction 8
2.2 Neuroelectromagnetic Forward and Inverse Problems 8
2.3 Regularization Techniques 13
2.4 Assessment Criteria of Source Estimation 14
2.5 Simulations and Results 15
2.5.1 Sources Contaminated by Brain Perturbation 16
2.5.2 Sensors Contaminated by Measurement Noise 21
3 Estimation of Correlated Neuroelectromagnetic Activities in Deep Source Space **26**
3.1 Introduction 26
3.2 Methods 28
3.2.1 Inverse Algorithms 28
3.2.2 Proposed Approach 29
3.3 Simulations and Results 31
3.3.1 Simulation Setups 31
3.3.2 Estimation Results of Localizations 36
3.3.3 Estimation Results of Activity Time Series 40
4 Reconstruction of Neuroelectromagnetic Source Connectivity Network **43**
4.1 Introduction 43
4.2 Methods 45
4.2.1 Granger Causality Connectivity Analysis 45
4.2.2 Inverse Algorithms 46
4.2.3 Proposed Approach 46
4.2.4 Reconstruction Process 48
4.3 Simulations and Results 49

4.3.1 Simulation Setups 49
4.3.2 Results of Reconstructed Time Series 53
4.3.3 Results of Reconstructed Connectivity Networks 56
5 Analysis of Neuroelectromagnetic Source Signal via Subspace Decomposition Imaging 60
5.1 Introduction 60
5.2 Subspace Decomposition Imaging Method 61
5.3 Verification by Simulation Studies 65
5.3.1 Two Typical Simulations 68
5.3.2 Simulation of Multi-varying Time Series 79
5.4 Application to Practical Measurements 85
5.5 Noise Suppression in MEG Measurement for Improving Neuroelectromagnetic Source Estimation 92
5.5.1 Method 93
5.5.2 Simulations and Results 96
6 Conclusion 101
References 105
초록 116
Acknowledgment 118

List of Figures

Figure 1-1 Thesis outline.....5
Figure 2-1 Neuroelectromagnetic forward problem.....11
Figure 2-2 Neuroelectromagnetic inverse problem.....12
Figure 2-3 Example of cortical patch activities. (a) Original sources with one activity. (b) Original sources with two activities. (c) Sources with one activity contaminated by brain perturbation (-12.065dB SNR). (d) Sources with two activities contaminated by brain perturbation (-1.763dB SNR).....17
Figure 2-4 Estimation results. (a) Estimated by the L-curve (one activity). (b) Estimated by GCV (one activity). (c) Estimated by the L-curve (two activities). (d) Estimated by GCV (two activities).....19
Figure 2-5 Scalp topographies of MEG data. (a) Original MEG data in the case of one activity. (b) Original MEG data in the case of two activities. (c) MEG data contaminated by measurement noise (-7.762dB SNR) in the case of one activity. (d) MEG data contaminated by measurement noise (-2.484dB SNR) in the case of two activities.....22
Figure 2-6 Estimation results. (a) Estimated by the L-curve (one activity). (b) Estimated by GCV (one activity). (c) Estimated by the L-curve (two activities). (d) Estimated by GCV (two activities).....23
Figure 3-1 Time series used for the simulations.....34
Figure 3-2 Simulated magnetic field recordings.....35
Figure 3-3 Estimation results obtained by assigning the *s2* and *s1* as the 1st and 2nd activity time series. Original locations of the activities are indicated by the small black dots. (a) Spatial filter. (b) Conventional linear estimation with identity weighting matrix. (c) Conventional linear estimation with weighting matrix R_s. (d) Proposed linear estimation with weighting matrix R_c.
.....37
Figure 3-4 Estimation results obtained by assigning the *s2* and *s3* as the 1st and 2nd activity time series. Original locations of the activities are indicated by the small black dots. (a) Spatial filter. (b) Conventional linear estimation with identity weighting matrix. (c) Conventional linear estimation with weighting matrix R_s. (d) Proposed linear estimation with weighting matrix R_c.
.....39
Figure 3-5 Estimated time series of the two activities obtained using the proposed method in the case of the low correlation.....41

Figure 3-6 Estimated time series of the two activities obtained using the proposed method in the case of the high correlation. 42
Figure 4-1 Time series used for the simulation. The blue, green and red lines indicate the series $s_x(t)$, $s_y(t)$ and $s_z(t)$, respectively. 50
Figure 4-2 Underlying source connectivity network. 52
Figure 4-3 Reconstructed time series of the three patch activities when the SNR is 10 dB. The black lines indicate the original time series. The blue, green and red lines indicate the reconstructed source time series obtained by the linear estimation, the spatial filter and the proposed approach, respectively. 54
Figure 5-1 Boundary element meshes generating. 66
Figure 5-2 Forward model building. 67
Figure 5-3 Original locations of two active sources. 69
Figure 5-4 Time series of active sources used for simulations and the simulated magnetic field recordings (A=0.2). 72
Figure 5-5 Source estimates obtained by MN, SDI: low-rank component and SDI: sparse component at 203ms (A=0.2). 73
Figure 5-6 Estimated source time series obtained by MN, SDI: sparse component and SDI: low-rank component (A=0.2). 74
Figure 5-7 Original source time series and the simulated magnetic field recordings (A=5). 76
Figure 5-8 Source estimates obtained by MN, SDI: low-rank component and SDI: sparse component at 203ms (A=5). 77
Figure 5-9 Estimated source time series obtained by MN, SDI: sparse component and SDI: low-rank component (A=5). 78
Figure 5-10 Multi-varying time series of active sources used for simulation. 81
Figure 5-11 Simulated magnetic field recordings. 82
Figure 5-12 Estimation results. 83
Figure 5-13 Estimated time series of the active sources. 84
Figure 5-14 Resection region. 86
Figure 5-15 Overall procedure of localizing epileptic activity. 87
Figure 5-16 MEG waveform of the epilepsy patient. 89
Figure 5-17 Estimated results of epileptic activity. 91
Figure 5-18 The overall procedure for solving the SDI-based noise suppression. 95
Figure 5-19 Simulation setups and results. (a) The locations and time series of the active sources. (b) The simulated electromagnetic field measurements

under -5 dB SNR. (c) The results (estimated source distributions at 227 *ms* and estimated source time series) via traditional method. (d) The results via proposed method. 98

List of Tables

Table 1 REs in the L-curve and GCV estimations (sources contaminated by brain perturbation).....20
Table 2 CCs in the L-curve and GCV estimations (sources contaminated by brain perturbation).....20
Table 3 REs in the L-curve and GCV estimations (sensors contaminated by measurement noise).....25
Table 4 CCs in the L-curve and GCV estimations (sensors contaminated by measurement noise).....25
Table 5 Values of the parameters used for generating *s1* and *s2* 33
Table 6 Correlations between the time series.....33
Table 7 Connectivity information of the time series.....51
Table 8 Error of the reconstructed time series 55
Table 9 Reconstructed connectivity network 57
Table 10 Error of the reconstructed connectivity network.....59
Table 11 DFs of the estimated source distributions 100
Table 12 CCs of the true and estimated time series 100

1 Introduction

Magnetoencephalography (MEG) is a common noninvasive biomedical technique used to measure weak electromagnetic fields generated by some ensembles of neurons inside the brain with high temporal resolution [1]. The main objective of neuroelectromagnetic source signal analysis is to accurately estimate the location, distribution of a neuronal signal at a fine time series resolution, and to provide functional information about source dynamics based on the outside electromagnetic field measurement [2-10].

To solve the inverse problem, the field is sampled at different sensor locations and the underlying activity pattern is then determined [11, 12]. In the case where no *a priori* information is known about the source to be estimated, a method named Moore-Penrose Inverse estimates the source signal solely by the outside measurement without any constraints [13, 14]. The minimum norm (MN) estimation minimizes the L2-norm of the estimated source in the sense that the overall intensity of the source current should be as low as possible. Unfortunately, this constraint is not necessarily physiologically valid because there is no proof that the source current configuration with the second lowest intensity is not actually the correct one. The MN estimation thus favors the superficial source that the deeper source will be incorrectly estimated on the shallower position than the actual situation [5]. In order to compensate for the disfavored deep source, various weighted minimum norm estimation (wMNE) methods have been developed by applying a weighting matrix to the

estimated source. The weighting matrix can have different forms but the simplest possible weighting is based on the norm of the columns of the lead field matrix, which has been shown to improve localization result [5, 10, 15]. The well known low-resolution electromagnetic tomography (LORETA) sets the weighting matrix to an approximation of the Laplacian operator and favors spatially smooth current distribution, however the spatial resolution of LORETA is blurry and relatively low [2, 16]. Two noise normalized MN estimation methods, dynamic statistical parametric mapping (dSPM) and standardized low-resolution electromagnetic tomography (sLORETA), which can implicitly perform depth weighting by a normalization with the estimated noise at each source [15, 17]. The variants of MN techniques mentioned above is appropriate for estimating spatially extended source. Nevertheless, intracranial experiments have demonstrated that the some neural activities are sparsely localized in the brain, such as early sensory activity and focal epilepsy [18, 19]. The MN based methods are not suitable for localization of spatially focal source since the minimum L2-norm constraint penalizes such estimates [20]. The Focal underdetermined system solver (FOCUSS) [21, 22] iteratively updates the weight according to the source estimated in previous step, leading to a more focal source estimate, but the drawback of the FOCUSS is its sensitivity to noise and initial estimated source [16, 20]. Moreover, the Lp-norm ($p \leqslant 2$) iterative sparse solution (LPISS) integrates the Lp-norm constraint for sparse source into the iterative procedure of FOCUSS. Compared with FOCUSS, LPISS forces the estimated source to converge to a sparse one effectively, however, it needs much more computation because of solving the Lp-norm constrained problem [23]. Another set of methods aimed

at providing bias toward sparse and focal sources use the L1-norm of the estimated source as a constraint. Such considerations yield several related optimization estimations. For instance, one of the most popular types is known as the minimum current estimation (MCE), which minimizes the sum of the source absolute current and leads to more focal source estimates than estimates using L2-norm [24, 25]. Over the years, this scheme and its modifications have been extensively studied by various authors. Huang et al. [26] present a vector based spatial-temporal analysis using a L1-minimum norm (VESTAL) to remedy the spatial "jumping" and temporal "spiky-looking" encountered in the conventional focal estimations. In the VESTAL approach, the temporal information of the outside measurement is used to enhance the stability of the estimated source. In an attempt to fix the orientation discrepancy problem arising in the L1-norm based methods, the sparse source imaging (SSI) technique which is achieved by the second order cone programming has been developed [27]. Based on the assumption that the source activity is sparse in the space-time plane, Bolstad et al. [16] develop an event sparse penalty procedure using the spatiotemporal framework. A solution space sparse coding optimization (3SCO) algorithm is taken by Xu et al. [3] in which the L0-norm constraint is introduced to guarantee the sparse source is estimated by using the particle swarm optimization procedure [28].

Finally, the choice of estimation methods can be different depends on the nature of brain activities in various conditions. L2-norm based estimations are suited to image diffuse source whereas L0 and L1-norm based estimations are suited to image focal source. Therefore, it is hard to find a universal estimation method to accurately image all kinds of brain activities, e.g.,

diffuse activities in cognitive tasks or spontaneous states, focal activities induced by somatosensory stimulation. The choice of estimation methods and the understanding of the nature of brain activities in different applications are the challenges in neuroelectromagnetic source imaging [29, 30]. In addition, as far as the estimation methods are concerned, we are not aware of the uncertain brain activity, e.g., composite activity. Recently, a novel compressive neuromagnetic tomography (CENT) method based on the assumption that the current sources are compressible is proposed. Instead of explicitly favoring either spatially more sparse or extended sources, the CENT method yields better estimate than the L1 or L2-norm methods when both focal and diffuse sources are present simultaneously [2].

As mentioned above, due to the widely recognized ill-posed nature of the neuroelectromagnetic inverse problem, the source signal estimation is not unique unless some possible and reasonable constraints are imposed [2, 3, 16, 30-33]. Consequently, in this thesis, various inverse algorithms are proposed to obtain an optimal resolution by adding computationally tractable and biophysically plausible constraints to the source signal imaging method.

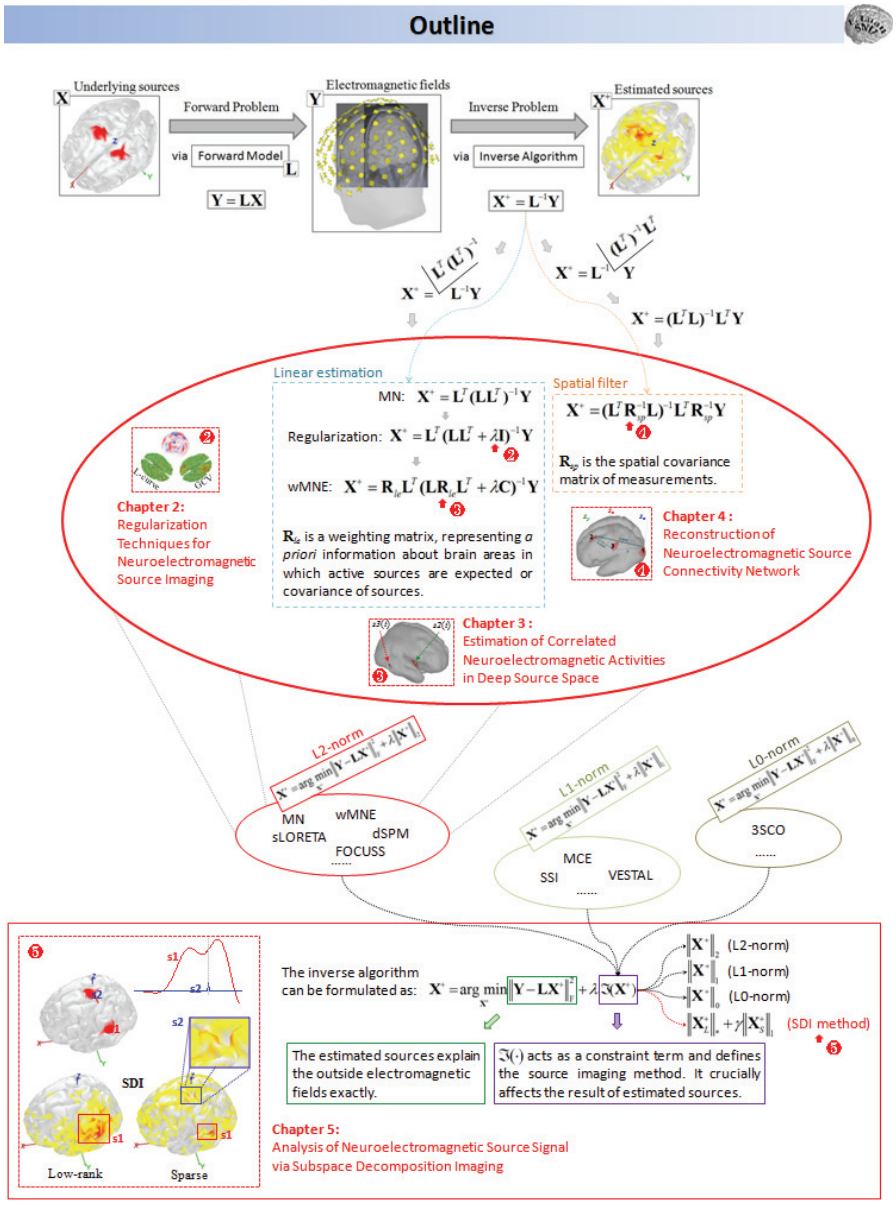

Figure 1-1 Thesis outline.

As shown in Figure 1-1, this thesis consists of 6 chapters. The remainder of the thesis is organized as follows. In chapter 2, the abilities of the generalized cross validation (GCV) method and the L-curve method for the determination of the optimal regularization parameter are studied and compared for neuroelectromagnetic source estimation. The results verify that the GCV method is a better choice when the measurement noise is relatively high, and the L-curve method seems to be more effective when the source is mainly dominated by errors such as brain perturbation.

In chapter 3, an improved inverse technique for precisely estimating the correlated neuroelectromagnetic activities in the deep source space is proposed. A novel weighting matrix building method obtained from the sensitivity similarity degree of the sensor array between the sources is presented, so as to enhance the property representation for the correlated deep sources. The results confirm that the proposed technique provides more detailed information for the source estimation, improves the result accuracy and is physically more reasonable than the conventional linear estimation and spatial filtering techniques.

Recent studies on neuroelectromagnetic inverse problems have shown that a satisfactory understanding of source mechanisms requires to perform source connectivity analyses. Chapter 4 focuses on the comparison of inverse techniques for reconstructing the source connectivity network. The results confirm that the noise effect for linear estimation technique is direct, while, for spatial filtering technique the effect is indirect. Linear estimation is advantageous for the connectivity reconstruction of high quality MEG data,

while, the benefit for the case of spatial filter is low signal-to-noise ratio (SNR) environments. This chapter also proposes a modified spatial filtering method to improve the source connectivity reconstruction by using the correlation gram matrix. The results show that the proposed method can increase the reconstruction accuracy, decrease the error fluctuation and enhance the representation for profiles of the original source connectivity network.

In chapter 5, a subspace decomposition imaging (SDI) method for measuring neuroelectromagnetic source signal is proposed. The SDI technique is based on spatiotemporal signal analysis from matrix perspective that decomposes the source into low-rank and sparse components in a manner consistent with underlying bio-mechanism in statistics. The results establish the feasibility of SDI method for neuroelectromagnetic source signal measurement, with resulting solutions that provide substantial performance improvement over conventional method. Moreover, noise suppression in MEG measurement is particularly challenging because it is difficult to remove the noise and preserve the information components in the MEG data. In this chapter, a novel noise suppression method, based on SDI technique, is also studied and applied to neuroelectromagnetic source estimation. The results show that the proposed method can significantly improve the estimation performance.

Finally, brief conclusion and future work are given in chapter 6.

2 Regularization Techniques for Neuroelectromagnetic Source Imaging

2.1 Introduction

In this chapter, the effectiveness of the generalized cross validation (GCV) and the L-curve methods for selecting the regularization parameter for neuroelectromagnetic inverse problem is assessed [34]. By considering two factors, sources contaminated by brain perturbations and sensors contaminated by measurement noise, the performance of these two methods is tested in terms of the intuitive comparison of the reconstructed cortical topography, and the quantitative comparison of the relative error (RE) and the correlation coefficient (CC) [35, 36]. Finally, through simulations, some guidelines are proposed for determining the optimal degree of regularization.

2.2 Neuroelectromagnetic Forward and Inverse Problems

As shown in Figure 2-1, the neuroelectromagnetic forward problem considers modeling the relationship between inside brain electrical sources and the outside electromagnetic fields [37], which is formulated in matrix notation as,

$$\mathbf{Y}=\mathbf{LX} \tag{2.1}$$

where $\mathbf{Y}$ is an $M \times T$ matrix of the outside electromagnetic measurement from M sensors at T time points, $\mathbf{L}$ is the $M \times D$ lead field matrix (or forward model), and $\mathbf{X}$ is the $D \times T$ matrix of the unknown source from D discrete dipole locations.

As shown in Figure 2-2, neuroelectromagnetic source imaging is an inverse problem of the formula (2.1). The estimation accuracy of the neuroelectromagnetic sources is crucially dependent on the conditioning of the lead field matrix to be inverted. However, the signals measured from the MEG have very small values, and thus they are easily influenced by various external disturbances and noise. Furthermore, because of the limited number of sensors, there is an underdetermined relationship between the sources and the sensors [38, 39]. For these reasons, the neuroelectromagnetic inverse problem is very often ill-posed, which means that there is not a single, well-behaved solution. The solution is very sensitive to even small perturbations in the measurement data and the brain model. Therefore, in order to prevent oscillatory behavior in the presence of noise, the development of a very robust inverse algorithm with an optimal regularization determination method is highly desired [40-43]. In such cases, the well-known Tikhonov regularization scheme is employed.

The regularized solution for the neuroelectromagnetic inverse problem in the absence of reliable *a priori* information about the generating sources can be formulated as,

$$\mathbf{X}^{+}=\arg\min_{\mathbf{X}^{+}}\left\|\mathbf{Y}-\mathbf{L}\mathbf{X}^{+}\right\|_{\mathrm{F}}^{2}+\lambda^{2}\left(\Im(\mathbf{X}^{+})\right)^{2} \tag{2.2}$$

where $\mathbf{X}^{+}$ is the $D\times T$ matrix of the estimated source, $\|\cdot\|_{\mathrm{F}}$ denotes the Frobenius norm, $\left\|\mathbf{Y}-\mathbf{L}\mathbf{X}^{+}\right\|_{\mathrm{F}}^{2}$ is a measure of the difference between the outside measured data $\mathbf{Y}$ and the data that would be obtained. $\lambda^{2}\left(\Im(\mathbf{X}^{+})\right)^{2}$ is a Tikhonov regularization term that penalizes large constraint solutions. λ denotes the regularization parameter, which controls the amount of regularization. The value of λ controls the properties of the regularized solution. In equation (2.2), $\Im(\cdot)$ acts as a constraint term and defines the imaging method. The choice of $\Im(\cdot)$ crucially affects the result of the estimated source [44].

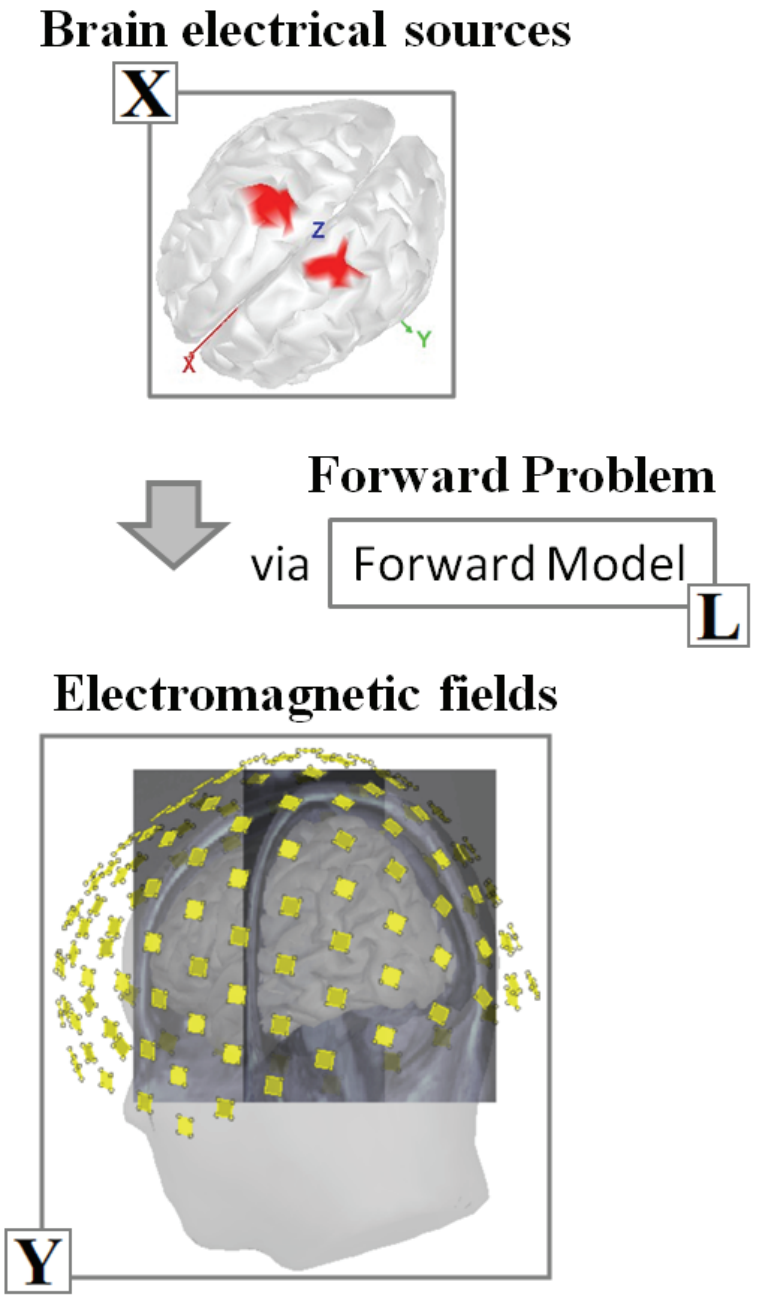

Figure 2-1 Neuroelectromagnetic forward problem.

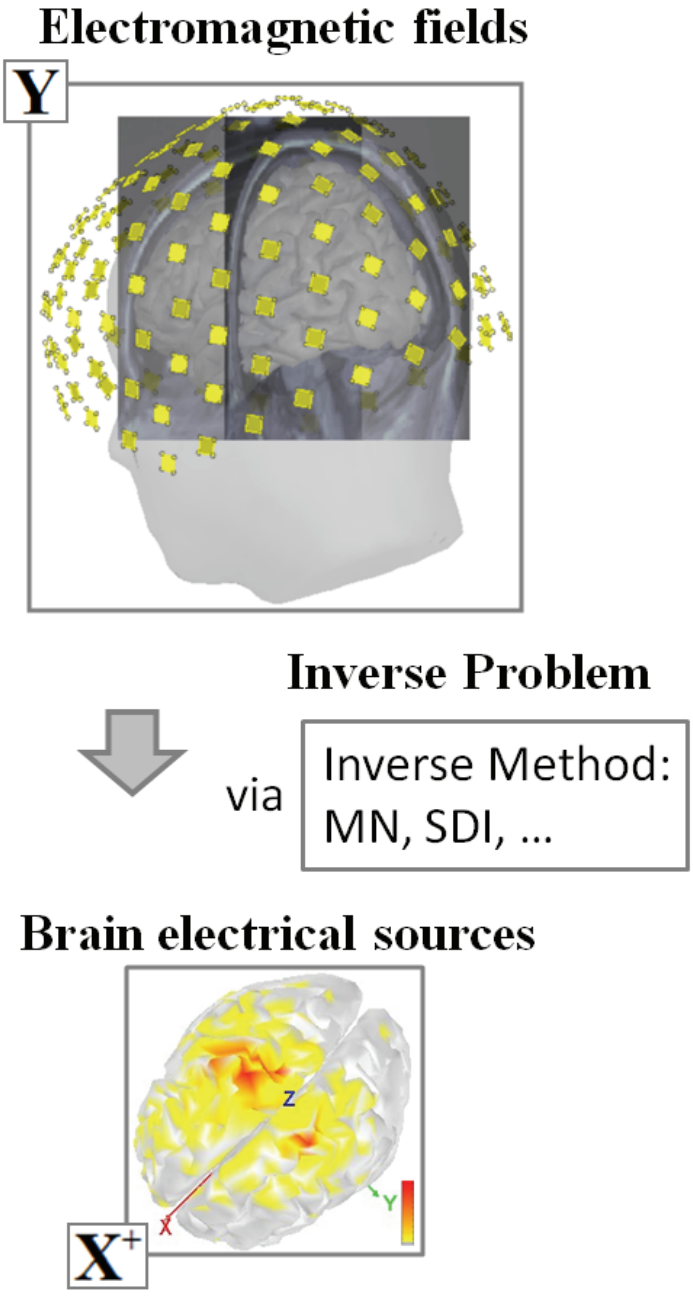

Figure 2-2 Neuroelectromagnetic inverse problem.

2.3 Regularization Techniques

The efficiency of Tikhonov regularization method is highly dependent on the proper choice of λ that produces a fair balance between the perturbation error and the regularization error [45-47]. If too much regularization is imposed, the result of the estimation will become less sensitive to perturbations in the data. On the other hand, if too little regularization is used, the estimation will be dominated by the contributions from various types of errors. However, the determination of the value of λ is not straightforward in practical applications without *a prior* knowledge of either the neuroelectromagnetic sources or the noise. Therefore, two methods have been widely used, the GCV method and the L-curve method, which do not require prior information in order to determine the optimal regularization parameter [48-50].

The GCV method is based on the principle that, if an arbitrary data point is left out, then the regularized solution should correctly estimate this missing data. This leads to the choosing of the regularization parameter which minimizes the GCV function,

$$\mathrm{GCV}(\lambda) = \frac{\left\| \mathbf{L}\mathbf{x}^{+} - \mathbf{y} \right\|_2^2}{[\mathrm{trace}(\mathbf{I} - \mathbf{L}\mathbf{L}_{regu})]^2} \tag{2.3}$$

where **y** is the vector of the outside electromagnetic measurement from M sensors at a time point, **x** is the vector of the unknown source from D discrete

dipole locations at a time point, $\mathbf{x}^+$ is the estimated vector of $\mathbf{x}$, and $\mathbf{L}_{regu}$ is a matrix which produces the $\mathbf{x}^+$ when multiplied with $\mathbf{y}$.

The L-curve method is a graphical tool with a log-log plot of $\|\mathbf{x}\|_2$ versus $\|\mathbf{L}\mathbf{x}-\mathbf{y}\|_2$ for all valid regularization parameters. The optimal value of regularization parameter can then be determined by choosing the point of maximum curvature on the graph. More details of the GCV and the L-curve methods are presented in [48-50].

2.4 Assessment Criteria of Source Estimation

In this chapter, the effectiveness of the GCV and the L-curve methods is evaluated by computing two indexes. The first one is the RE, computed according to the formula,

$$\mathrm{RE} = \frac{\|\mathbf{x}^+ - \mathbf{x}\|_2}{\|\mathbf{x}\|_2} \tag{2.4}$$

where $\mathbf{x}$ represents the vector of the true sources, $\mathbf{x}^+$ denotes the reconstructed sources, and $\|\ \|_2$ is the standard L2-norm. The second one is the CC between $\mathbf{x}$ and $\mathbf{x}^+$, according the formula,

$$CC = \frac{\mathbf{x}^{+} \bullet \mathbf{x}}{\sqrt{\left\|\mathbf{x}^{+}\right\|_2^2 \cdot \left\|\mathbf{x}\right\|_2^2}} \tag{2.5}$$

where $\bullet$ stands for the inner product. A larger CC implies that the stronger pairs of the true and reconstructed sources are related.

2.5 Simulations and Results

The performance of the inverse algorithm is hard to verify by *in vivo* experiments because the exact underlying sources inside of a real human brain cannot be estimated *a priori*. Therefore, we resort to a simulation with known source configurations implemented in MATLAB. The system configurations for the simulations use 151-channel sensors (axial gradiometers) on MEG machine. Furthermore, to utilize anatomical information, the interface between white and grey matter is extracted from magnetic resonance imaging (MRI) T1 images of a standard brain and tessellated to build the source space (10004 source dipoles) [51]. Each possible cortical source is represented by a current dipole oriented normal to the cortical surface, i.e., both the location and orientation are constrained by the cortical surface. A spherical homogeneous volume conductor model is made as the electromagnetic field model in order to compute the external fields and scalp potentials for a specific set of brain electrical sources. It is obvious that the use of the realistic head model enhances the solution accuracy, but the spherical head model has

been widely used, especially for MEG simulation studies, considering computational cost [52]. We then artificially construct forward data sets, assuming a single activity and two simultaneous activities. In the simulation here, we define $\Im(\cdot)$ in (2.2) as Frobenius norm.

2.5.1 Sources Contaminated by Brain Perturbation

In this section, practical aspects of two regularization parameter determination methods are related as to the level of sources contaminated by brain perturbations and the accuracy of reconstruction. Before the forward calculation, brain perturbations are added to the original source signals, to reach different levels of SNR. Figure 2-3 shows an example of the assumed cortical patch activities, Figures 2-3(a) and (b) are the original sources with one and two activities, Figures 2-3(c) and (d) show examples of the sources contaminated by brain perturbations in the case of one and two activities. Then, after calculating the forward problem, we construct the artificial MEG measurement data. The validation consists of the estimation of the source distribution with the regularization parameters provided by the GCV and L-curve methods taken from the MEG data.

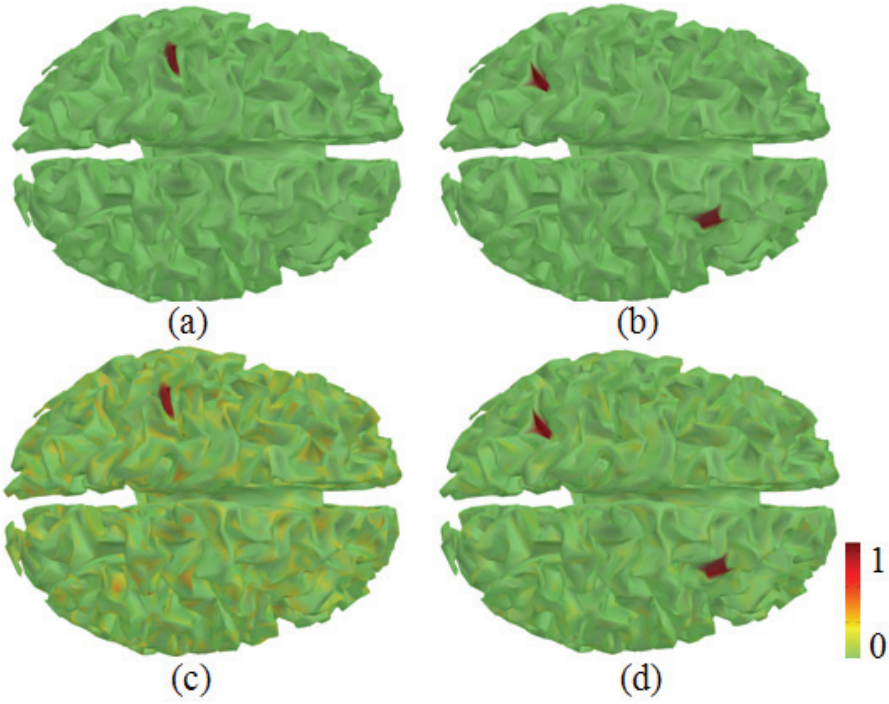

Figure 2-3 Example of cortical patch activities. (a) Original sources with one activity. (b) Original sources with two activities. (c) Sources with one activity contaminated by brain perturbation (-12.065dB SNR). (d) Sources with two activities contaminated by brain perturbation (-1.763dB SNR).

Figures 2-4(a) and (b) show the source distribution of a single activity estimated at a -12.065dB SNR of brain perturbation by the L-curve and the GCV. Figures 2-4(c) and (d) show the source distribution of two activities estimated at a -1.763dB SNR of brain perturbation by the L-curve and the GCV, respectively. As illustrated, the locations of the unknown activities are revealed with the estimated source distributions obtained from the two methods. However, the efficiency of the L-cure and GCV cannot be determined easily, just as in the case of direct intuitive comparisons of the figures.

For more quantitative comparisons, the REs and CCs are evaluated from 9000 repeated simulations, assuming seven levels of brain perturbations. As shown in Table 1, we can see the L-curve appears to give a better choice of the regularization parameter for the estimation than the GCV since the RE of the estimated source distribution is smaller over the range having a low SNR, although the difference is very small. As the SNR of the sources decreased the L-curve method produces more successful estimation results than the GCV method because of the larger CC, as shown in the Table 2. In the next section, the capability of the GCV method is demonstrated and compared to that of the L-curve when the sensors are dominated by measurement noise.

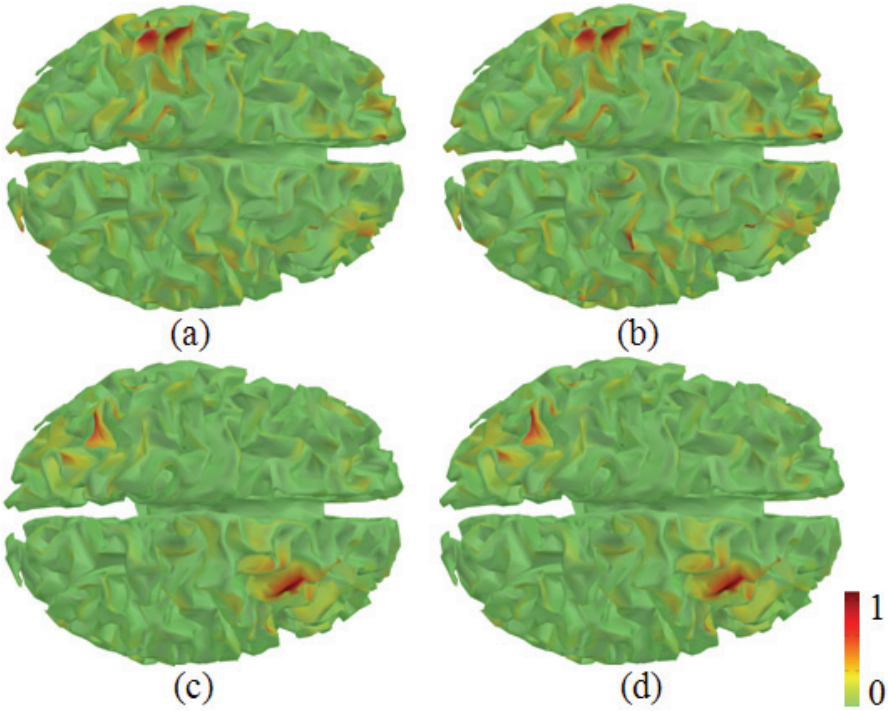

Figure 2-4 Estimation results. (a) Estimated by the L-curve (one activity). (b) Estimated by GCV (one activity). (c) Estimated by the L-curve (two activities). (d) Estimated by GCV (two activities).

Table 1 REs in the L-curve and GCV estimations (sources contaminated by brain perturbation)

One Activity			Two Activities		
SNR (dB)	RE		SNR (dB)	RE	
	L-curve	GCV		L-curve	GCV
28.451	0.977	0.977	30.790	0.967	0.967
8.449	0.978	0.978	10.790	0.968	0.968
-3.592	0.981	0.981	-1.251	0.970	0.970
-10.635	0.994	0.995	-7.272	0.977	0.977
-11.550	0.998	0.999	-8.294	0.979	0.979
-15.073	1.023	1.025	-12.732	0.997	0.998
-17.570	1.056	1.061	-15.230	1.018	1.020

Table 2 CCs in the L-curve and GCV estimations (sources contaminated by brain perturbation)

One Activity			Two Activities		
SNR (dB)	CC		SNR (dB)	CC	
	L-curve	GCV		L-curve	GCV
28.451	0.253	0.253	30.790	0.293	0.293
8.449	0.250	0.250	10.790	0.291	0.291
-3.592	0.211	0.210	-1.251	0.271	0.271
-10.635	0.137	0.135	-7.272	0.221	0.221
-11.550	0.126	0.124	-8.294	0.208	0.208
-15.073	0.087	0.084	-12.732	0.141	0.141
-17.570	0.064	0.062	-15.230	0.105	0.104

2.5.2 Sensors Contaminated by Measurement Noise

Since contamination caused by various kinds of errors in the measurements is inevitable, as an extension to the simulations presented in previous section, the sensor data are contaminated by different levels of artificial measurement noise, in order to compare directly the abilities of the two methods in this different noise environment. Figure 2-5 shows the assumed scalp topographies of the sensors, Figures 2-5(a) and (b) show the original sensor data of the single and the double activities, Figures 2-5(c) and (d) show an example of the sensors contaminated by measurement noise in the cases of a -7.762dB SNR (one activity) and a -2.484dB SNR (two activities).

Figure 2-6 shows the reconstructed sources applied to the example shown in Figure 2-5. Figures 2-6(a) and (b) show the source distribution (one activity) estimated at the -7.762dB SNR of measurement noise by the L-curve and the GCV. Figures 2-6(c) and (d) show the source distribution (two activities) estimated at the -2.484dB SNR of measurement noise by the two methods. It can be seen from the figures that the source distributions obtained from the L-curve method are discontinuous and include many noisy sources, and the location of the unknown activities cannot be found. On the contrary, the GCV method seems to be more robust than the L-curve because a more focused source distribution with less spurious sources is obtained from the GCV method and the activities can be observed.

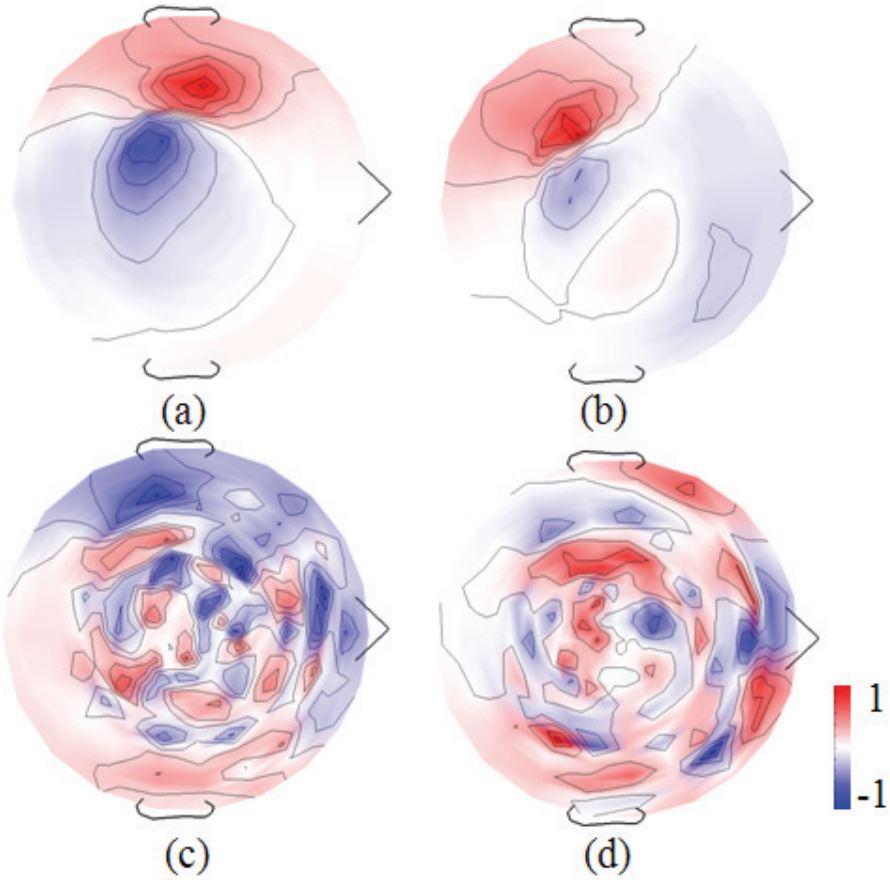

Figure 2-5 Scalp topographies of MEG data. (a) Original MEG data in the case of one activity. (b) Original MEG data in the case of two activities. (c) MEG data contaminated by measurement noise (-7.762dB SNR) in the case of one activity. (d) MEG data contaminated by measurement noise (-2.484dB SNR) in the case of two activities.

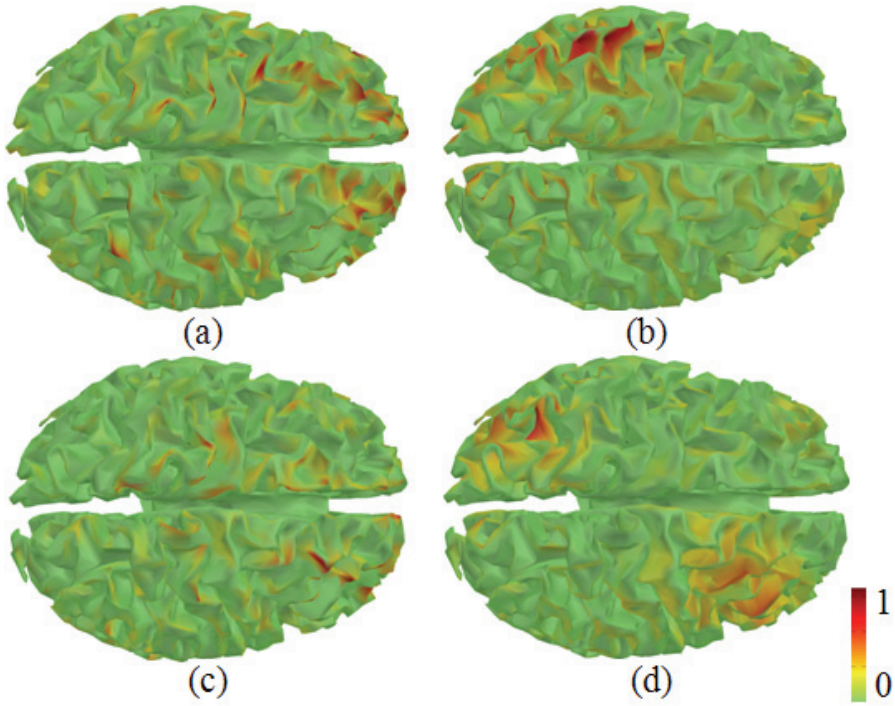

Figure 2-6 Estimation results. (a) Estimated by the L-curve (one activity). (b) Estimated by GCV (one activity). (c) Estimated by the L-curve (two activities). (d) Estimated by GCV (two activities).

To synthesize the results more quantitatively, Tables 3 and 4 show the variations of the RE and the CC evaluated from 9000 repeated simulations, respectively. We can see from the tables that the evaluation results produced by the L-curve and GCV are almost same in the regions with relatively low level measurement noise, but the accuracy of the L-curve gets worse as the level of measurement noise becomes higher, e.g., SNR = -2.020, -8.052, -12.908, and -16.004dB, in the case of one activity. However, the RE and the CC of the GCV method are not affected much by the measurement noise as compared to the L-curve. Similar trends are found in the case having two activities, e.g., SNR = -2.980 and -4.552dB.

We can conclude from these comparisons that it appears that the GCV method is a better choice for estimating optimal regularization parameter when the MEG source reconstruction results are mainly dominated by measurement noise. However, the L-curve can be a more effective method when the brain perturbation levels are relatively high.

Table 3 REs in the L-curve and GCV estimations (sensors contaminated by measurement noise)

One Activity			Two Activities		
SNR	RE		SNR	RE	
(dB)	L-curve	GCV	(dB)	L-curve	GCV
63.989	0.978	0.977	64.993	0.969	0.968
43.996	0.979	0.979	44.988	0.972	0.973
23.990	0.982	0.987	24.985	0.978	0.982
-2.020	2.719	0.999	1.473	1.127	1.012
-8.052	76.063	1.013	-1.036	1.869	1.010
-12.908	203.967	1.066	-2.980	4.244	1.015
-16.004	301.654	1.063	-4.552	11.664	1.004

Table 4 CCs in the L-curve and GCV estimations (sensors contaminated by measurement noise)

One Activity			Two Activities		
SNR	CC		SNR	CC	
(dB)	L-curve	GCV	(dB)	L-curve	GCV
63.989	0.249	0.251	64.993	0.287	0.287
43.996	0.231	0.244	44.988	0.259	0.265
23.990	0.222	0.223	24.985	0.238	0.240
-2.020	0.127	0.146	1.473	0.164	0.163
-8.052	0.026	0.112	-1.036	0.140	0.150
-12.908	-0.001	0.082	-2.980	0.112	0.140
-16.004	-0.003	0.061	-4.552	0.084	0.131

3 Estimation of Correlated Neuroelectromagnetic Activities in Deep Source Space

3.1 Introduction

Studies of cognitive functions and resting state networks require estimation of electromagnetic activities emanating from deep source space, such as the hippocampus and thalamus. However, since the activities from deep source space are poorly represented in MEG signals, and their electromagnetic fields drop rapidly with distance, the challenge of the electromagnetic activities estimation lies in the limited sensitivity to the deep source space [30, 53].

To solve electromagnetic inverse problems, various approaches for estimating spatiotemporal activities have been proposed. Among such approaches, two class inverse algorithms called linear estimation and spatial filter have been widely used recently [7, 54, 55]. The well-known weakness of spatial filter is that it requires a large number of recordings time samples to build recordings covariance matrix, therefore, it can hardly be applied to single time sample data [56]. Another weakness common to the spatial filter is the significant degradation in performance in the presence of high correlated activities [57]. In this chapter, we focus on the linear estimation technique, which does not suffer from these weaknesses. Generally, the linear estimation requires a weighting matrix to represent the metric associated with the knowledge about locations or relationships of sources [14]. However, this knowledge cannot be

determined *a priori* by electromagnetic nondestructive methods, the conventional linear estimations have usually assumed that all source activities are completely uncorrelated, which means that relationships between neighboring sources are ignored. When using the conventional linear estimations, the estimated amplitude for a source at the deep locations is always weaker than actual [17]. Furthermore, the deeper an activity lies and the more it is surrounded by anisotropic sources [51], the more complex source relationships influence on the inverse estimation. Since a satisfactory understanding of the functional mechanism between different activities requires consideration of the complex relationships [58], an appropriate relationship should be taken into account when building the weighting matrix to improve the quality of the source estimation. Towards this goal, the geometrical information, such as, the Euclidean distance and the three-dimensional geodesic distance of the adjacent sources, is used to make the artificial relationship [54]. Indeed, the appropriate weighting matrix should be designed in order to reflect the desired property of the sources. In other words, when estimating the temporarily correlated source activities, we should plan this property with respect to the correlation [59].

This chapter suggests a modified linear inverse operator with a proposed weighting matrix obtained from the relationship between electromagnetic flux densities and dipole sources so as to reflect the correlation property of the sources. This approach is applied to the realistic MEG simulations and the results demonstrate that the proposed approach can estimate the correlated deep activities more precisely than the conventional linear estimation and spatial filtering techniques.

3.2 Methods

3.2.1 Inverse Algorithms

The expression for the linear inverse operator **W** is,

$$\mathbf{W} = (\mathbf{LRL}^T + \mathbf{C})^{-1}\mathbf{LR}, \quad \mathbf{X}^+ = \mathbf{W}^T\mathbf{Y} \tag{3.1}$$

where **R** is the weighting matrix and **C** is the noise covariance matrix [60]. In the conventional linear estimations, the relationships between the neighboring sources are assumed to be ignored, which means that the weighting matrix is a diagonal matrix. If the activity can be expected at any location in the source space equally, this diagonal matrix becomes identity matrix [14]. Otherwise, the $\boldsymbol{l}(d)$ can be imposed to each diagonal entry of the weighting matrix [61], then $\mathbf{R}_s$ is expressed as,

$$\mathbf{R}_s = \begin{bmatrix} \|\boldsymbol{l}(I)\|_2^2 & 0 & \cdots & 0 & \cdots & 0 \\ 0 & \|\boldsymbol{l}(2)\|_2^2 & \cdots & 0 & \cdots & 0 \\ \vdots & \vdots & \ddots & \vdots & \iddots & \vdots \\ 0 & 0 & \cdots & \|\boldsymbol{l}(d)\|_2^2 & \cdots & 0 \\ \vdots & \vdots & \iddots & \vdots & \ddots & \vdots \\ 0 & 0 & \cdots & 0 & \cdots & \|\boldsymbol{l}(D)\|_2^2 \end{bmatrix} \tag{3.2}$$

where D is the number of sources, $\|\boldsymbol{l}\|_2$ is the standard L2-norm of a vector $\boldsymbol{l}$, and $\boldsymbol{l}$ will be explained hereunder.

3.2.2 Proposed Approach

The recording of the mth sensor is denoted as $l_m(d)$ when a single unit-magnitude source exists at the dth volume element of the source space, therefore, $l_m(d)$ indicates the sensitivity of the mth sensor to a source located at the dth volume element. The vector $\boldsymbol{l}(d) = [l_1(d), l_2(d), \cdots, l_m(d), \cdots, l_M(d)]^{\mathrm{T}}$ expresses the sensitivity of the whole sensor array for the mth unit-magnitude source, here M is the number of sensors, and this sensitivity information can be revealed by using the lead field matrix

$$\mathbf{L} = \begin{bmatrix} l_1(1) & l_1(2) & \cdots & l_1(d) & \cdots & l_1(D) \\ l_2(1) & l_2(1) & \cdots & l_2(d) & \cdots & l_2(D) \\ \vdots & \vdots & \ddots & \vdots & \iddots & \vdots \\ l_m(1) & l_m(2) & \cdots & l_m(d) & \cdots & l_m(D) \\ \vdots & \vdots & \iddots & \vdots & \ddots & \vdots \\ l_M(1) & l_M(2) & \cdots & l_M(d) & \cdots & l_M(D) \end{bmatrix} = \begin{bmatrix} \boldsymbol{l}(1) & \boldsymbol{l}(2) & \cdots & \boldsymbol{l}(d) & \cdots & \boldsymbol{l}(D) \end{bmatrix} \tag{3.3}$$

Physically, the deeper an activity source is located, the more it is surrounded by other sources, and the more complex relationships will influence on the

final inverse resolution. Since close similar $\boldsymbol{l}$ s have larger relationship and mutual effect, in order to improve the estimation quality, those influencing factors should be taken into account when building the weighting matrix. In this chapter, the source relationship is defined as the similarity degree of the sensitivities of the whole sensor array for the neighboring sources, thereby the weighting matrix is expressed as,

$$\mathbf{R}_c = \begin{bmatrix} R_{1,1} & R_{1,2} & \cdots & R_{1,j} & \cdots & R_{1,D} \\ R_{2,1} & R_{2,2} & \cdots & R_{2,j} & \cdots & R_{2,D} \\ \vdots & \vdots & \ddots & \vdots & \iddots & \vdots \\ R_{i,1} & R_{i,2} & \cdots & R_{i,j} & \cdots & R_{d,D} \\ \vdots & \vdots & \iddots & \vdots & \ddots & \vdots \\ R_{D,1} & R_{D,2} & \cdots & R_{D,j} & \cdots & R_{D,D} \end{bmatrix} \tag{3.4}$$

$$R_{i,j} = \frac{\boldsymbol{l}(i) \bullet \boldsymbol{l}(j)}{\|\boldsymbol{l}(i)\|_2 \cdot \|\boldsymbol{l}(j)\|_2}$$

$R_{i,j}$ reveals MEG recording similarity degree between the *i*th and *j*th sources.

3.3 Simulations and Results

3.3.1 Simulation Setups

Original locations of two point active sources indicated by small black dots in Figure 3-3 are selected in order to represent the locations in the deep source space. The time series are generated according to the following model,

$$s(t) = \Re \cdot e^{-\left(\frac{t-\tau}{\Omega}\right)^2} \cdot \sin[2\pi \cdot f \cdot (t-\Delta)] \tag{3.5}$$

where $\Re$, τ, Ω, f and Δ are the parameters controlling the shapes of the time series. The values of these parameters used in this chapter are listed in Table 5. Time series $s1(t)$ and $s2(t)$ at 1 *ms* intervals from 1 to 375 *ms* are shown in blue and green broken lines in Figure 3-1. The third time series calculated using,

$$s3(t) = \xi \cdot s1(t) + \zeta \cdot s2(t) \tag{3.6}$$

where parameter ξ and ζ control the degree of correlation between $s3(t)$ and $s2(t)$. Time series $s3(t)$ when $\xi = 0.5$, $\zeta = 0.25$ is shown by the red broken line in Figure 3-1. In this case, the correlation information between any pair of the three time series are shown in Table 6.

The simulated magnetic recordings shown in Figure 3-2 are calculated by assigning the $s1(t)$ and $s2(t)$ to the 1st and 2nd activities in Figure 3-3, respectively, when the overlapping spheres model is used as the forward model.

Table 5 Values of the parameters used for generating *s1* and *s2*

	$\Re(pA.m)$	$\tau\ (ms)$	$\Omega\,(ms)$	$f\,(kHz)$	$\Delta\,(ms)$
s1	25	63.5625	205.3125	0.0101	130.3125
s2	50	98.7188	230.6250	0.0169	115.3125

Table 6 Correlations between the time series

	s1-s2	*s1-s3*	*s2-s3*
Correlation coefficient	0.0890	0.6671	0.8014

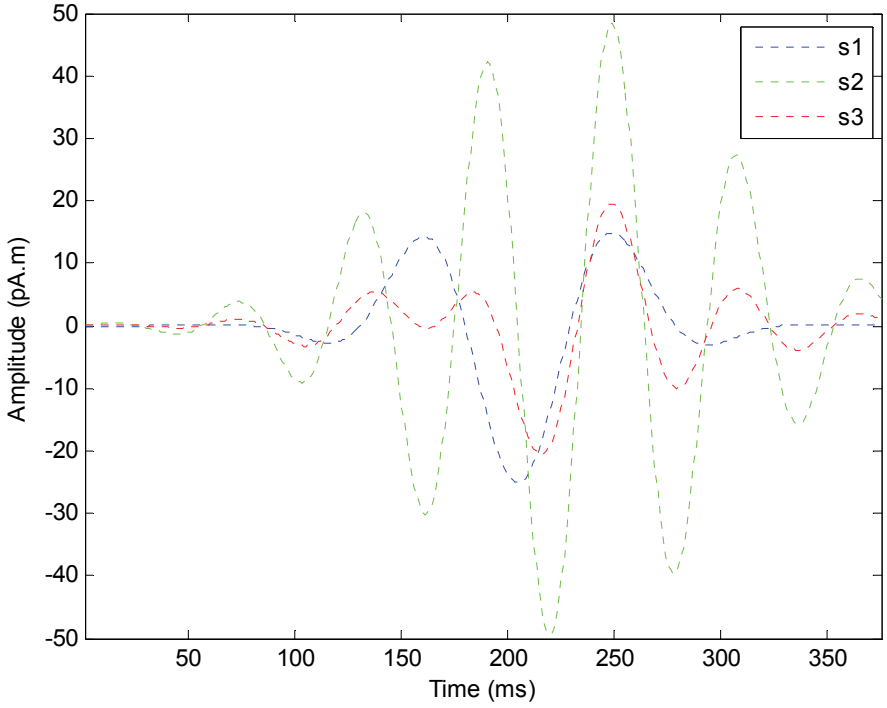

Figure 3-1 Time series used for the simulations.

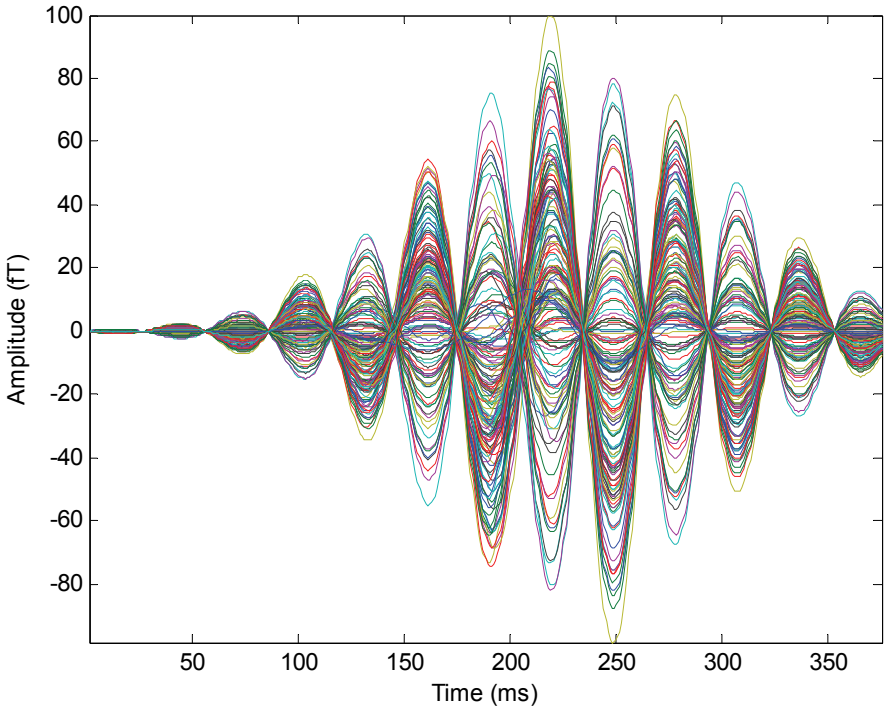

Figure 3-2 Simulated magnetic field recordings.

3.3.2 Estimation Results of Localizations

The source estimation is performed by using the three linear inverse operators and the spatial filter. Here, the spatial filter is chosen for comparison, because it is a method representative of another popular estimation technique. The source distribution (average over the time series), is estimated by using the *s2* and *s1* as the 1st and 2nd point activity time series, and the results are displayed in Figure 3-3. It can be clearly seen that the proposed inverse operator estimated the two deep activities at the correct locations. On the contrary, other methods failed to localize the 1st and 2nd activities. From the intuitive comparisons, we can evidently observe that the proposed technique is able to precisely estimate the correlated activities in the deep source space.

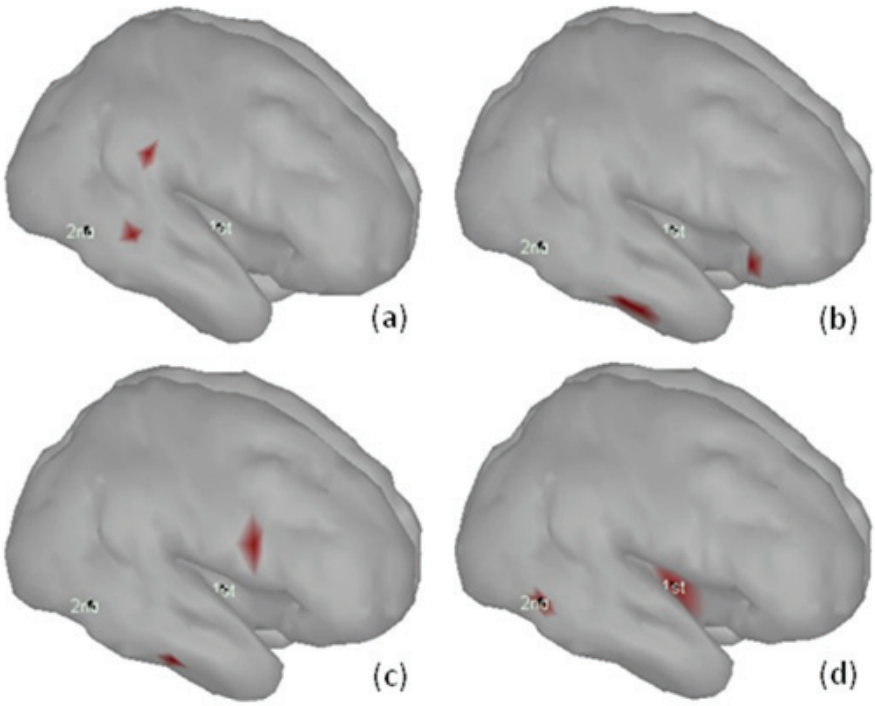

Figure 3-3 Estimation results obtained by assigning the *s2* and *s1* as the 1st and 2nd activity time series. Original locations of the activities are indicated by the small black dots. (a) Spatial filter. (b) Conventional linear estimation with identity weighting matrix. (c) Conventional linear estimation with weighting matrix $\mathbf{R}_s$. (d) Proposed linear estimation with weighting matrix $\mathbf{R}_c$.

In the previous simulation, the temporal correlation of the 1st and 2nd activities is low, i.e., correlation coefficient is 0.0890 as shown in Table 6. We then perform simulations in which activities are highly correlated, thereby, checking the sensitivity of the inverse methods to the correlation. Without changing the time series of the 1st activity, we assign the time series *s3* to the 2nd activity. In this case, the correlation coefficient between the two activities turned out to be 0.8014. The estimation results of high correlated activities is shown in Figure 3-4. Despite the localization accuracy, it can be seen that the results obtained from three linear estimations are identical with those of Figure 3-3, suggesting that the linear estimations are not influenced by the source correlation. However, as shown in Figures 3-3(a) and 3-4(a), the result of the spatial filter shows a severe influence from the source correlation, i.e., the estimation results of the two cases are significantly different. On the other hand, the proposed inverse operator seems to be very effective and stable because two activities are again well localized even though they are highly correlated, as illustrated in Figure 3-4(d).

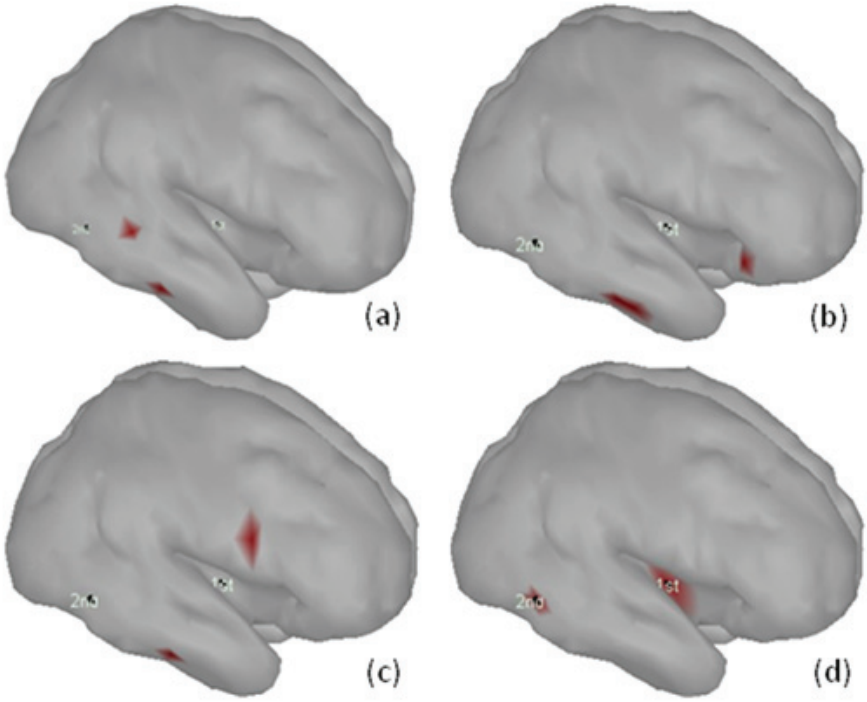

Figure 3-4 Estimation results obtained by assigning the *s2* and *s3* as the 1st and 2nd activity time series. Original locations of the activities are indicated by the small black dots. (a) Spatial filter. (b) Conventional linear estimation with identity weighting matrix. (c) Conventional linear estimation with weighting matrix $\mathbf{R}_s$. (d) Proposed linear estimation with weighting matrix $\mathbf{R}_c$.

3.3.3 Estimation Results of Activity Time Series

The estimated time series of the activity obtained by the proposed linear estimation in the cases of low and high correlations are shown in Figures 3-5 and 3-6, respectively. Here, the estimated activities are the point sources that give the local maxima in Figures 3-3(d) and 3-4(d). As shown in Figures 3-5 and 3-6, the broken and solid green lines are almost overlapped, indicating that the proposed method is valid for retrieving the original *s2* time series for the 1st activity. However, since the original time series of the 2nd activity are weaker than that of the 1st activity, the estimated time series for the 2nd activities are distorted in varying degrees as shown in Figures 3-5 and 3-6. Yet we should note that compared with the distortion in the case of low correlation (see blue lines in Figure 3-5), the distortion in the case of high correlation (see red lines in Figure 3-6) is relatively slight, the reason for this is the compensating effect of the high correlation from the 1st activity. The results demonstrate that the proposed estimation can provide almost accurate time series estimation for the strong signal of the deep activity, nearly accurate estimation for the weak activity in the case of high correlated with the strong one, and distort time series estimation for the weak activity which is low correlated with the strong one.

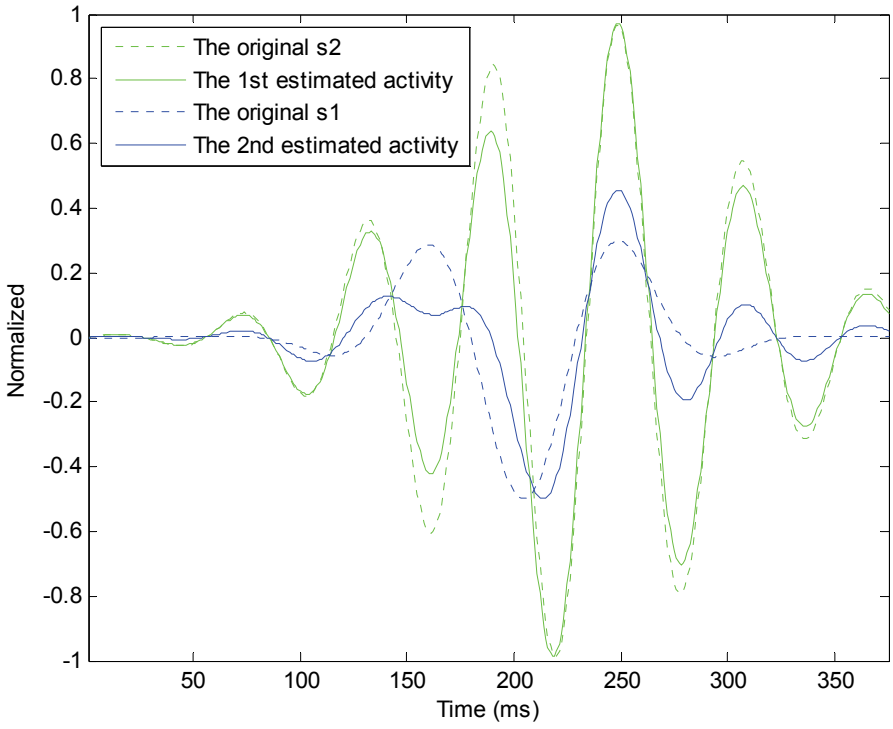

Figure 3-5 Estimated time series of the two activities obtained using the proposed method in the case of the low correlation.

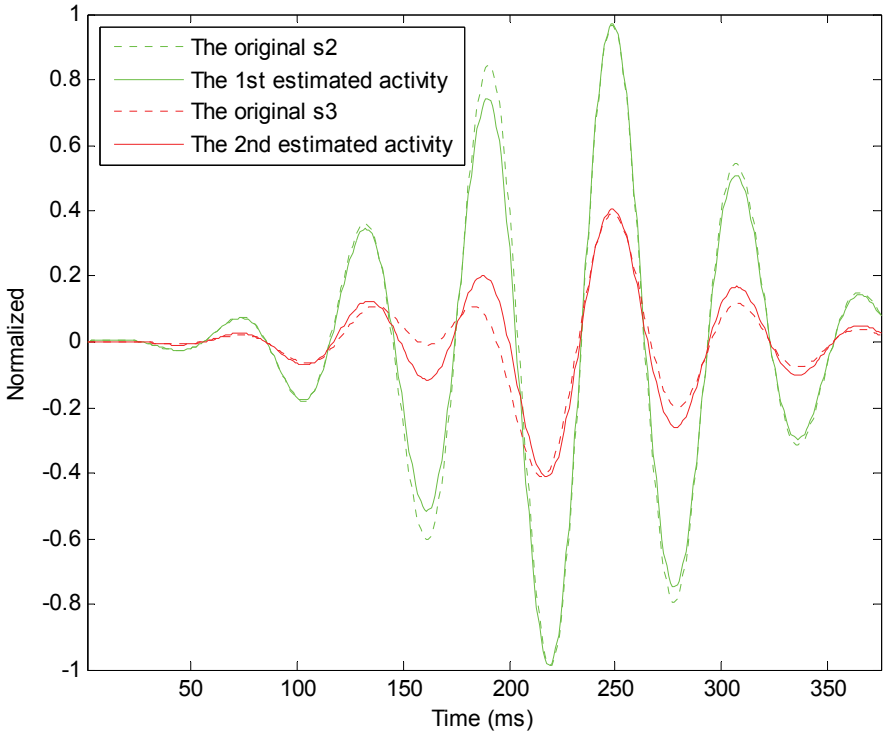

Figure 3-6 Estimated time series of the two activities obtained using the proposed method in the case of the high correlation.

4 Reconstruction of Neuroelectromagnetic Source Connectivity Network

4.1 Introduction

The traditional studies of the MEG source reconstruction have been proposed to localize the activities and study such activity-specific changes in isolation, however, this isolated study is insufficient. A satisfactory understanding of the source mechanisms requires measuring of relationship analyses between activities [30, 58, 62]. Many methods for connectivity analyses have been proposed, e.g. synchrony, coherence, and Granger [63-65]. Among these methods, synchrony and coherence are used to assess undirected connectivity. Granger can reveal information about direction and degree of connectivity and is widely used by several groups [58, 64]. One benefit of MEG is that it can extract the time series of the sensor level measurement with excellent temporal resolution [66], therefore, MEG is a very promising tool to investigate the sensor level connectivity. However, MEG measurement is sensitive to the field spread effect, the connectivity analyses at the sensor level cannot generate straightforward interpretations at the source level. Another benefit of MEG is that it can estimate the activities with good spatial resolution, thereby, MEG source connectivity network reconstruction is becoming main issue in the neuroelectromagnetic inverse computation researches recently [58, 63, 66-73].

The inverse techniques can effectively reduce the field spread effect, and have been successfully used to MEG source reconstruction problems. Although inverse algorithms are constantly being improved and different methods have been comprehensively compared [56], most comparisons mainly focus on localization bias or spatial resolution instead of fully comparing unique source connectivity reconstruction characteristics [6, 34, 39, 74, 75]. Thus, a complete and rigorous comparison of the performance of inverse techniques for MEG source connectivity network reconstruction is placing increasing demands. There are two popular types of inverse techniques. One class is the linear estimation based technique whose result mainly depends on the measurement geometry and the source covariance matrix. Another class is the minimum variance spatial filtering technique, the result of which depends on the measurement geometry as well as the covariance matrix of the measurement [56, 74].

This chapter evaluates two inverse algorithms, with respect to the effectiveness of the MEG source connectivity network reconstruction. By considering the reconstructed source series, the reconstructed connectivity strength and the violation by the measurement noise, a thorough comparison is performed when the underlying sources condition is in a connectivity network form. This chapter also suggests a modified spatial filter with a proposed correlation gram matrix to improve the reconstruction result. Finally, through simulations, some guidelines are proposed for a consensus on using inverse algorithms of the source connectivity network reconstruction.

4.2 Methods

4.2.1 Granger Causality Connectivity Analysis

Granger causality implements a statistical interpretation of directed connectivity in which *U* causes *V* if knowing the past of *U* can help predict the future of *V*, better than knowing the past of *V* alone. Granger causality can identify the directed functional connectivity, and give a satisfactory understanding of neural mechanisms. To calculate Granger causality, suppose that the temporal connectivity of two time series $u(t)$ and $v(t)$ can be estimated by the following models,

$$\begin{aligned} u(t) &= \sum_{i=1}^{O} A(i)u(t-i) + e_u(t) \\ v(t) &= \sum_{i=1}^{P} B(i)v(t-i) + \sum_{i=1}^{Q} C(i)u(t-i) + e_v(t) \end{aligned} \tag{4.1}$$

where *A*, *B* and *C* contain the model coefficients, *O*, *P* and *Q* (the model orders) represent the number of considered past time points, e_u and e_v are the regression residuals (prediction errors) for each time series. The magnitude of connectivity in the direction of $u(t)$ causes $v(t)$, for instance, is the log ratio of the prediction error variances for the restricted (omitting time series $u(t)$ in the autoregressive model of $v(t)$) and full models (refer to [64, 76, 77] for more details).

4.2.2 Inverse Algorithms

The expression for the inverse operator $\mathbf{W}_{le}$ according to the linear estimation is rewritten as follows,

$$\mathbf{W}_{le} = (\mathbf{L}\mathbf{R}_{le}\mathbf{L}^T + \mathbf{C})^{-1}\mathbf{L}\mathbf{R}_{le}, \quad \mathbf{X}^+ = \mathbf{W}_{le}^T\mathbf{Y} \tag{4.2}$$

where $\mathbf{R}_{le}$ is the weighting matrix according to the linear estimation, and $\mathbf{C}$ is the noise covariance matrix. Using the spatial filtering technique, the resultant inverse operator $\mathbf{W}_{sp}$ is derived as,

$$\mathbf{W}_{sp} = \mathbf{R}_{sp}^{-1}\mathbf{L}(\mathbf{L}^T\mathbf{R}_{sp}^{-1}\mathbf{L})^{-1}, \quad \mathbf{X}^+ = \mathbf{W}_{sp}^T\mathbf{Y} \tag{4.3}$$

$\mathbf{R}_{sp}$ is the spatial covariance matrix of the measurement [56, 74].

4.2.3 Proposed Approach

We denote the output of the *m*th sensor at time *t* as $y_t(m)$, the vector $\boldsymbol{y}(m) = [y_1(m) \quad y_2(m) \quad \cdots \quad y_t(m) \quad \cdots \quad y_T(m)]$ expresses the whole time series (from *1* to *T*) of the *m*th sensor output, and $\mathbf{Y}$ is,

$$\mathbf{Y} = \begin{bmatrix} y_1(1) & y_2(1) & \cdots & y_t(1) & \cdots & y_T(1) \\ y_1(2) & y_2(2) & \cdots & y_t(2) & \cdots & y_T(2) \\ \vdots & \vdots & \ddots & \vdots & \iddots & \vdots \\ y_1(m) & y_2(m) & \cdots & y_t(m) & \cdots & y_T(m) \\ \vdots & \vdots & \iddots & \vdots & \ddots & \vdots \\ y_1(M) & y_2(M) & \cdots & y_t(M) & \cdots & y_T(M) \end{bmatrix} = \begin{bmatrix} \boldsymbol{y}(1) & \boldsymbol{y}(2) & \cdots & \boldsymbol{y}(m) & \cdots & \boldsymbol{y}(M) \end{bmatrix}^T \tag{4.4}$$

where M is the number of sensors. The inverse operator $\mathbf{W}_{pa}$ of the proposed approach is then obtained by substituting $\mathbf{R}_{pa}$ for $\mathbf{R}_{sp}$ in (4.3),

$$\mathbf{W}_{pa} = \mathbf{R}_{pa}^{-1}\mathbf{L}(\mathbf{L}^T\mathbf{R}_{pa}^{-1}\mathbf{L})^{-1}, \quad \mathbf{X}^+ = \mathbf{W}_{pa}^T\mathbf{Y} \tag{4.5}$$

$\mathbf{R}_{pa}$ is the correlation gram matrix, defined as,

$$\mathbf{R}_{pa} = \begin{bmatrix} R_{1,1} & R_{1,2} & \cdots & R_{1,m} & \cdots & R_{1,M} \\ R_{2,1} & R_{2,2} & \cdots & R_{2,m} & \cdots & R_{2,M} \\ \vdots & \vdots & \ddots & \vdots & \iddots & \vdots \\ R_{m,1} & R_{m,2} & \cdots & R_{m,m} & \cdots & R_{m,M} \\ \vdots & \vdots & \iddots & \vdots & \ddots & \vdots \\ R_{M,1} & R_{M,2} & \cdots & R_{M,j} & \cdots & R_{M,M} \end{bmatrix} \tag{4.6}$$

$$R_{i,j} = \frac{\boldsymbol{y}(i) \bullet \boldsymbol{y}(j)}{\|\boldsymbol{y}(i)\|_2 \cdot \|\boldsymbol{y}(j)\|_2}$$

$R_{i,j}$ reveals the similarity degree between the *i*th and the *j*th sensor measurements.

4.2.4 Reconstruction Process

The detailed process of the connectivity network reconstruction is as follows.

Step 1) The locations of the patch source activities are selected on the cortical surface.

Step 2) Data generated by an autoregressive model are assigned as the time series to the activities.

Step 3) The underlying source connectivity is revealed by using the Granger causality.

Step 4) Source time series are employed to generate MEG sensor measurements by using forward computation.

Step 5) Inverse algorithms are used to estimate the source time series considering cortical connectivity.

Step 6) The estimated source time series are analyzed for connectivity, the reconstructed source connectivity is projected onto the cortical surface.

Step 7) The adequacy of inverse techniques are evaluated by comparing the difference between the reconstructed and the underlying connectivity networks.

4.3 Simulations and Results

4.3.1 Simulation Setups

Three extended patch source activities shown in Figure 4-2 are selected on the cortical surface in order to represent the locations of the occipital lobe tip, the top of the central sulcus, and the deeper insula. Three time series $s_x(t)$, $s_y(t)$ and $s_z(t)$, as shown in Figure 4-1, according to the following autoregressive model are assigned as activity time series to the sources 1, 2 and 3.

$$\begin{aligned} s_x(t) &= 0.6\,s_x(t-1) + 0.65\,s_y(t-2) \\ s_y(t) &= 0.5\,s_y(t-1) - 0.3\,s_y(t-2) - 0.3\,s_z(t-4) \\ s_z(t) &= 0.8\,s_z(t-1) - 0.7\,s_z(t-2) \end{aligned} \quad (4.7)$$

The connectivity information of the time series revealed by the Granger causality is shown in Table 7. The network form connectivity of the sources, shown in Figure 4-2, is considered as the underlying true source connectivity network. The arrow reveals the connectivity direction, the source 3 causes 2, and 2 causes 1. The width of solid line points out the connectivity strength, which means the connectivity strength of the source 2 to 1, i.e. 0.4070 is stronger than that of 3 to 2, i.e. 0.1634. The dash line indicates there is no connectivity between the endpoints, i.e. the connectivity strength of sources 3 and 1 is 0. An overlapping spheres model is applied for the forward calculation of the magnetic fields. Gaussian noise with SNR values (15, 10, 5, 3 dB) are added to MEG sensors to represent the range of the inevitable noise.

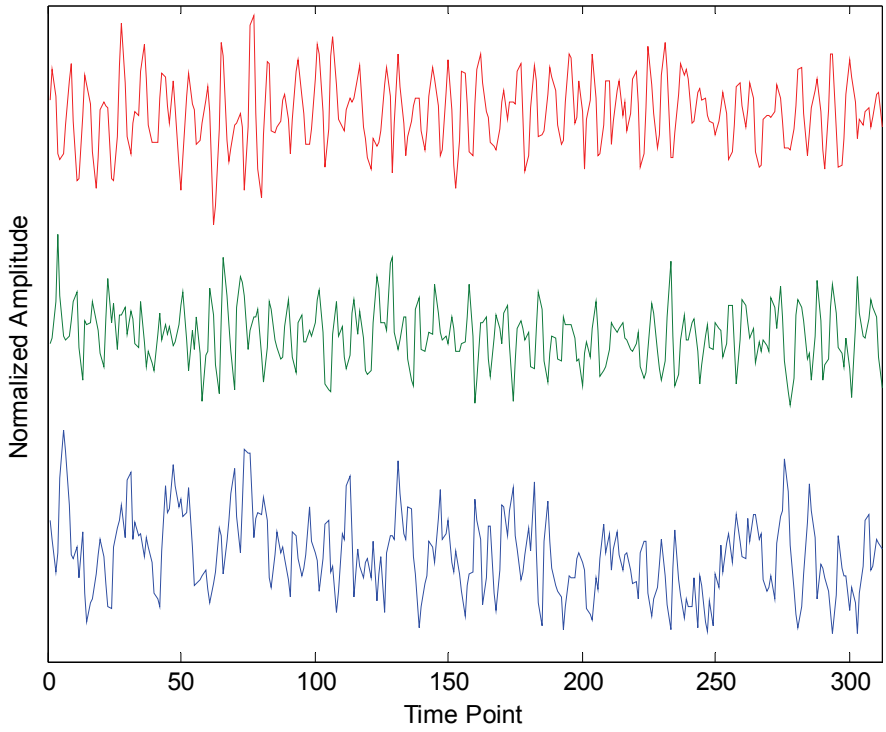

Figure 4-1 Time series used for the simulation. The blue, green and red lines indicate the series $s_x(t)$, $s_y(t)$ and $s_z(t)$, respectively.

Table 7 Connectivity information of the time series

Direction	Connectivity Strength
$\boldsymbol{s}_y \rightarrow \boldsymbol{s}_x$	0.4070
$\boldsymbol{s}_z \rightarrow \boldsymbol{s}_x$	0
$\boldsymbol{s}_z \rightarrow \boldsymbol{s}_y$	0.1634

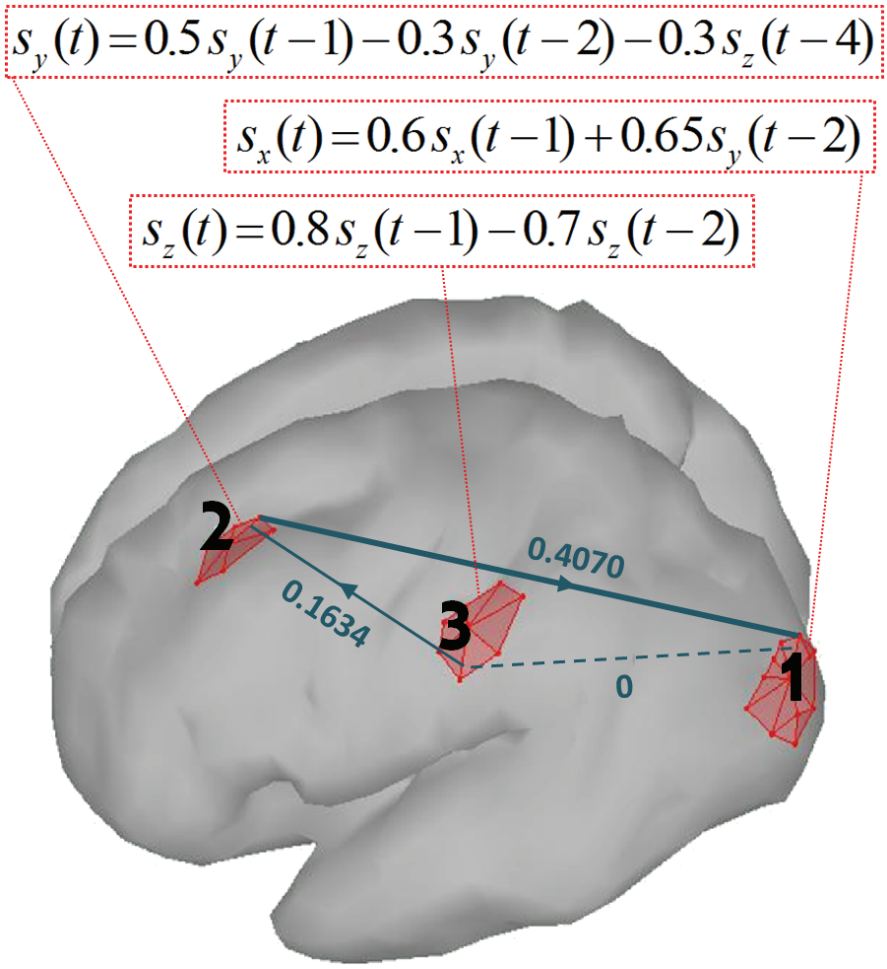

Figure 4-2 Underlying source connectivity network.

4.3.2 Results of Reconstructed Time Series

The source time series are the precondition for connectivity network reconstruction. We first reconstruct the source time series at the three locations of interest using the linear estimation, the spatial filter and the proposed approach. Figure 4-3 shows the reconstructed time series when the SNR is 10 dB. As can be seen, the black and red lines are almost overlapped, indicating that the proposed approach is valid for retrieving the original time series. The time series obtained by the linear estimation and the spatial filter shown in blue and green lines are distorted.

In order to quantitatively compare the performance of the inverse methods, the error of reconstructed time series is defined as the sum of absolute difference between the reconstructed and the original series at each time point. We can see that the proposed approach appears to give a better result than the other methods since the error of the reconstructed time series is smaller over the whole SNR range, as shown in Table 8. The results confirm that the proposed approach can increase the accuracy of the source time series reconstruction when the underlying sources are in the form of a connectivity network.

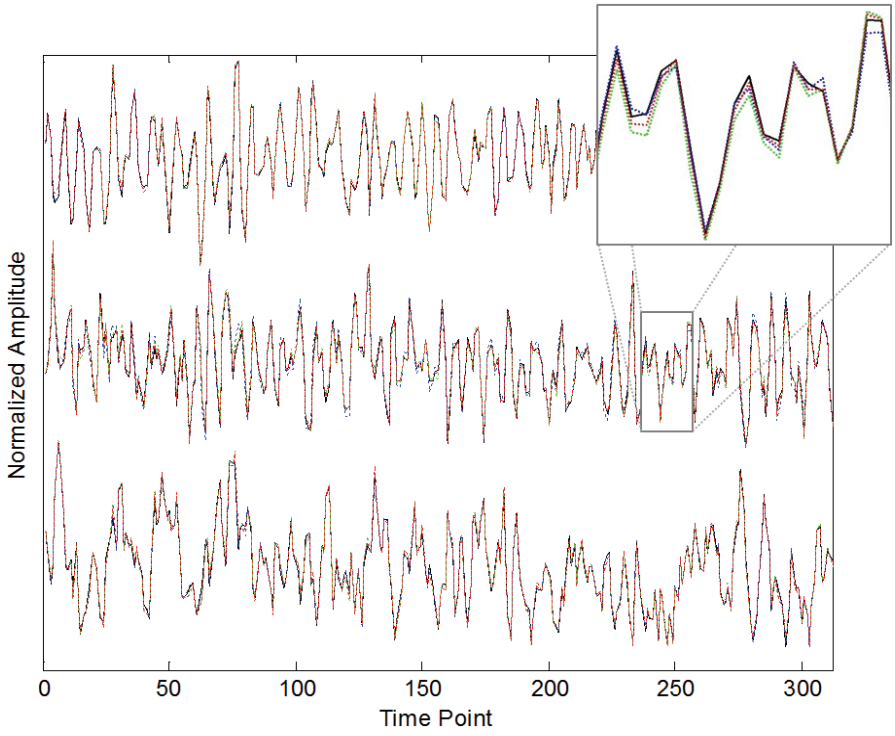

Figure 4-3 Reconstructed time series of the three patch activities when the SNR is 10 dB. The black lines indicate the original time series. The blue, green and red lines indicate the reconstructed source time series obtained by the linear estimation, the spatial filter and the proposed approach, respectively.

Table 8 Error of the reconstructed time series

SNR (dB)	Linear Estimation	Spatial Filter	Proposed Approach
15	7.2248	8.8882	6.4940
10	9.0557	9.3821	7.4533
5	11.1950	10.6023	9.6889
3	12.2879	11.4894	11.1104

4.3.3 Results of Reconstructed Connectivity Networks

Next, the Granger connectivity measure is applied to the reconstructed source time series. Table 9 shows the reconstructed connectivity network of the three activities, where "$i \rightarrow j$" represents the connectivity direction from the activity i to j. As shown, the underlying connectivity network can be revealed by all three inverse techniques, however, the reconstructed connectivity magnitudes from the proposed approach are in closer agreement with the underlying truth than those from the linear estimation and the spatial filter. This indicates that the use of correlation gram matrix can prevent the inclusion of spurious connectivity degree in the reconstructed connectivity network.

Table 9 Reconstructed connectivity network

SNR (dB)	Direction	Connectivity Strength		
		Linear Estimation	Spatial Filter	Proposed Approach
15	2 → 1	0.4041	0.3808	0.4015
	3 → 1	0	0	0
	3 → 2	0.1530	0.1527	0.1562
10	2 → 1	0.4102	0.3844	0.4053
	3 → 1	0	0	0
	3 → 2	0.1484	0.1529	0.1568
5	2 → 1	0.4186	0.4121	0.4088
	3 → 1	0	0	0
	3 → 2	0.1445	0.1428	0.1572
3	2 → 1	0.4222	0.4148	0.4087
	3 → 1	0	0	0
	3 → 2	0.1427	0.1420	0.1567

In order to examine the trends of the resultant connectivity networks obtained by different inverse algorithms, the reconstruction error is defined as the L2-norm of the difference between the reconstructed and the underlying true connectivity. As shown in Table 10, for the linear estimation, there is an increase in reconstruction error as SNR decreases. This reflects the direct pattern of noise effect on the source connectivity network reconstruction of the linear estimation. At high SNRs (15 and 10 dB) the results of the linear estimation are better than those of the spatial filter, while at low SNRs (5 and 3 dB) the linear estimation shows worse results than the spatial filter. For the spatial filter, the results at low SNRs are better than those at high SNRs, which shows a somewhat reversed pattern compared to the linear estimation. Hence, we can point out that the noise cannot influence the source connectivity network reconstruction directly when using the spatial filter. Moreover, the proposed approach has lower error than other two methods for all SNR cases, also, the error fluctuates within a narrow range. This leads to the fact that the proposed approach can contribute robust abilities to the connectivity network reconstruction.

Table 10 Error of the reconstructed connectivity network

SNR (dB)	L2-Norm Error (%)		
	Linear Estimation	Spatial Filter	Proposed Approach
15	2.46	6.45	2.07
10	3.50	5.68	1.55
5	5.06	4.84	1.47
3	5.86	5.19	1.58

5 Analysis of Neuroelectromagnetic Source Signal via Subspace Decomposition Imaging

5.1 Introduction

A subspace decomposition imaging (SDI) method for analysis of neuroelectromagnetic source signals is proposed in this chapter. The SDI technique can capture dynamic details in the source space that would sometimes be too weak to be recognized by conventional methods, but can also recover the stationary source signal contaminated by large brain perturbation. The SDI method is motivated by the conclusion of recent biomedical study that the neuronal signals have low intrinsic dimensionality, i.e., they lie on some low-dimensional subspace, or they are sparse [16, 78]. Naturally, the source can be separated into two components, in this situation, none of the above mentioned estimation algorithms is desirable. This brings us to the work shown in this chapter, which aims to address the following problems. Can we develop a source estimating algorithm that a better estimated result can be obtained when we decompose the source into low-rank and sparse components, assuming the underlying source is a superposition of those two, and simultaneously use these two as the constraints in some computationally tractable algorithm to the source imaging problem [79]. This is the main contribution of this chapter.

5.2 Subspace Decomposition Imaging Method

The inverse solution for the neuroelectromagnetic source imaging can be formulated as,

$$\mathbf{X}^{+} = \arg\min_{\mathbf{X}^{+}} \left\| \mathbf{Y} - \mathbf{L}\mathbf{X}^{+} \right\|_{\mathrm{F}}^{2} \tag{5.1}$$

The SDI method proposes a novel decomposition source model from the matrix perspective. Mathematically, this means the source matrix is the superposition of a low-rank matrix and a sparse matrix. Therefore, every source distribution $\mathbf{X}$ can be separated into parts $\mathbf{X}_L$ and $\mathbf{X}_S$ such that,

$$\mathbf{X} = \mathbf{X}_L + \mathbf{X}_S \tag{5.2}$$

where $\mathbf{X}_L$ has low rank and $\mathbf{X}_S$ is sparse. Obviously, the component $\mathbf{X}_L$ is stable over time with respect to the component $\mathbf{X}_S$ in the source space. If we require that two components explain the outside measurement exactly, the forward problem can be modeled as,

$$\mathbf{Y} = \mathbf{L}(\mathbf{X}_L + \mathbf{X}_S) \tag{5.3}$$

For the source signal imaging problem, we do not know the source matrix $\mathbf{X}$, not even the low-dimensional subspace of $\mathbf{X}_L$ as well as the locations and number of the nonzero entries of $\mathbf{X}_S$. The SDI algorithm is defined as the following constrained minimization of a cost function,

$$\begin{aligned} &\min_{\mathbf{X}_L^+, \mathbf{X}_S^+} \left\|\mathbf{X}_L^+\right\|_* + \gamma \left\|\mathbf{X}_S^+\right\|_1 \\ &\textit{subject to} \;\; \mathbf{Y} = \mathbf{L}(\mathbf{X}_L^+ + \mathbf{X}_S^+) \end{aligned} \tag{5.4}$$

where $\|\cdot\|_*$ denotes the matrix nuclear norm, i.e., the sum of singular values, $\|\cdot\|_1$ denotes the L1 norm, i.e., the sum of the absolute values of matrix entries, $\mathbf{X}_L^+$ is the estimated low-rank source matrix, $\mathbf{X}_S^+$ is the estimated sparse source matrix, and γ is a positive weighting parameter to balance the two terms,

$$\gamma = \frac{1}{\sqrt{\max(D, T)}} \tag{5.5}$$

The SDI algorithm recovers low-rank and sparse sources via the following optimization,

$$\left(\mathbf{X}_L^+, \mathbf{X}_S^+\right) = \arg\min_{\mathbf{X}_L^+, \mathbf{X}_S^+} \frac{\mu}{2}\left\|\mathbf{Y} - \mathbf{L}(\mathbf{X}_L^+ + \mathbf{X}_S^+)\right\|_{\mathrm{F}}^2 + \left\|\mathbf{X}_L^+\right\|_* + \gamma\left\|\mathbf{X}_S^+\right\|_1 \tag{5.6}$$

where μ is the parameter to be determined. There are several algorithms for solving this optimization problem [80-84]. In this work, the SDI adopts a fast and accurate algorithm for the low-rank and sparse decomposition, namely the augmented Lagrange multiplier (ALM) method [81]. The ALM method operates on the augmented Lagrangian,

$$\begin{aligned} L\left(\mathbf{X}_L^+, \mathbf{X}_S^+, \mathbf{L}_A, \mu\right) = {} & \left\|\mathbf{X}_L^+\right\|_* + \gamma\left\|\mathbf{X}_S^+\right\|_1 \\ & + \left\langle \mathbf{L}_A, \mathbf{X}^+ - \mathbf{X}_L^+ - \mathbf{X}_S^+ \right\rangle \\ & + \frac{\mu}{2}\left\|\mathbf{Y} - \mathbf{F}(\mathbf{X}_L^+ + \mathbf{X}_S^+)\right\|_{\mathrm{F}}^2 \end{aligned} \tag{5.7}$$

where $\mathbf{L}_A$ is the Lagrange multiplier matrix and $\langle \cdot \rangle$ denotes the standard trace inner product. Specifically, equation (5.4) can be practically solved by repeatedly minimizing equation (5.7) with respect to $\mathbf{X}_L^+$,

$$\arg\min_{\mathbf{X}_{L_{k+1}}^+} L(\mathbf{X}_{L_{k+1}}^+, \mathbf{X}_{S_k}^+, \mathbf{L}_{A_k}, \mu_k) = U\left(\Gamma_{\mu_k^{-1}}[S]\right)V^T \tag{5.8}$$

where $(U,S,V^T)=\text{svd}\left(\mathbf{X}^+-\mathbf{X}_{S_k}^+ +\mu_k^{-1}\mathbf{L}_{A_k}\right)$, $\mathbf{L}_{A_k}$ is the Lagrange multiplier matrix at the iteration time *k*, $\Gamma_\varepsilon[x]$ is the shrinkage operator,

$$\Gamma_\varepsilon[x]=\begin{cases}x-\varepsilon, \text{if } x>\varepsilon\\ x+\varepsilon, \text{if } x<-\varepsilon\\ 0, \text{otherwise}\end{cases} \tag{5.9}$$

where ε is a positive value. This operator can be extended to vectors and matrices by applying it element-wise.

Then minimizing equation (5.7) with respect to $\mathbf{X}_S^+$,

$$\arg\min_{\mathbf{X}_{S_{k+1}}^+} L(\mathbf{X}_{L_{k+1}}^+,\mathbf{X}_{S_{k+1}}^+,\mathbf{L}_{A_k},\mu_k)= \Gamma_{\lambda\mu_k^{-1}}\left[\mathbf{X}^+-\mathbf{X}_{L_k}^+ +\mu_k^{-1}\mathbf{L}_{A_k}\right] \tag{5.10}$$

equation (5.8) is an update of $\mathbf{X}_{L_{k+1}}^+$ and equation (5.10) is an update of $\mathbf{X}_{S_{k+1}}^+$ in the iterative ALM method loop.

Finally updating $\mathbf{L}_A$ based on the residual $\mathbf{X}^+-\mathbf{X}_L^+-\mathbf{X}_S^+$,

$$\mathbf{L}_{A_{k+1}}=\mathbf{L}_{A_k}+\mu_k\left(\mathbf{X}^+-\mathbf{X}_{L_{k+1}}^+-\mathbf{X}_{S_{k+1}}^+\right) \tag{5.11}$$

as well as updating μ by

$$\mu_{k+1} = 1.5\mu_k . \tag{5.12}$$

The repetition will terminate when the number of successive iterations without improvements in $\mathbf{X}_L^+$ and $\mathbf{X}_S^+$ reaches a specified number.

5.3 Verification by Simulation Studies

In the following simulations, implementations of SDI is described that optimally exploits the strengths of this method, and allows for efficient data processing, detailed analysis of results, and visualization. The system configurations for the simulation use whole-head MEG system, which consists of 306 channels arranged in triplets of two planar gradiometers (204 channels) and one magnetometer (102 channels). The interface between white and grey matter is extracted from MRI T1 standard brain images and tessellated into 3502 elements to build the cortical surface. As shown in Figures 5-1 and 5-2, the present study applied a boundary element method (BEM) model for the forward calculation of MEG measurements.

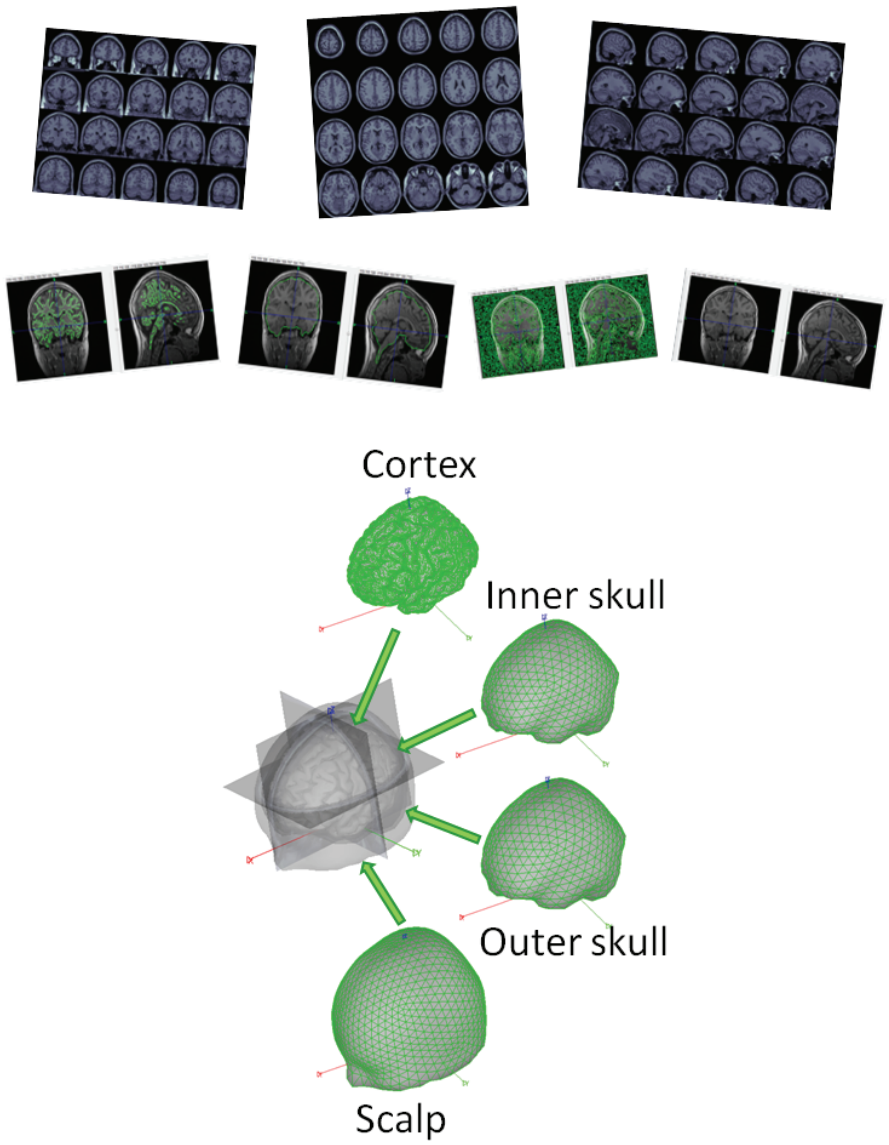

Figure 5-1 Boundary element meshes generating.

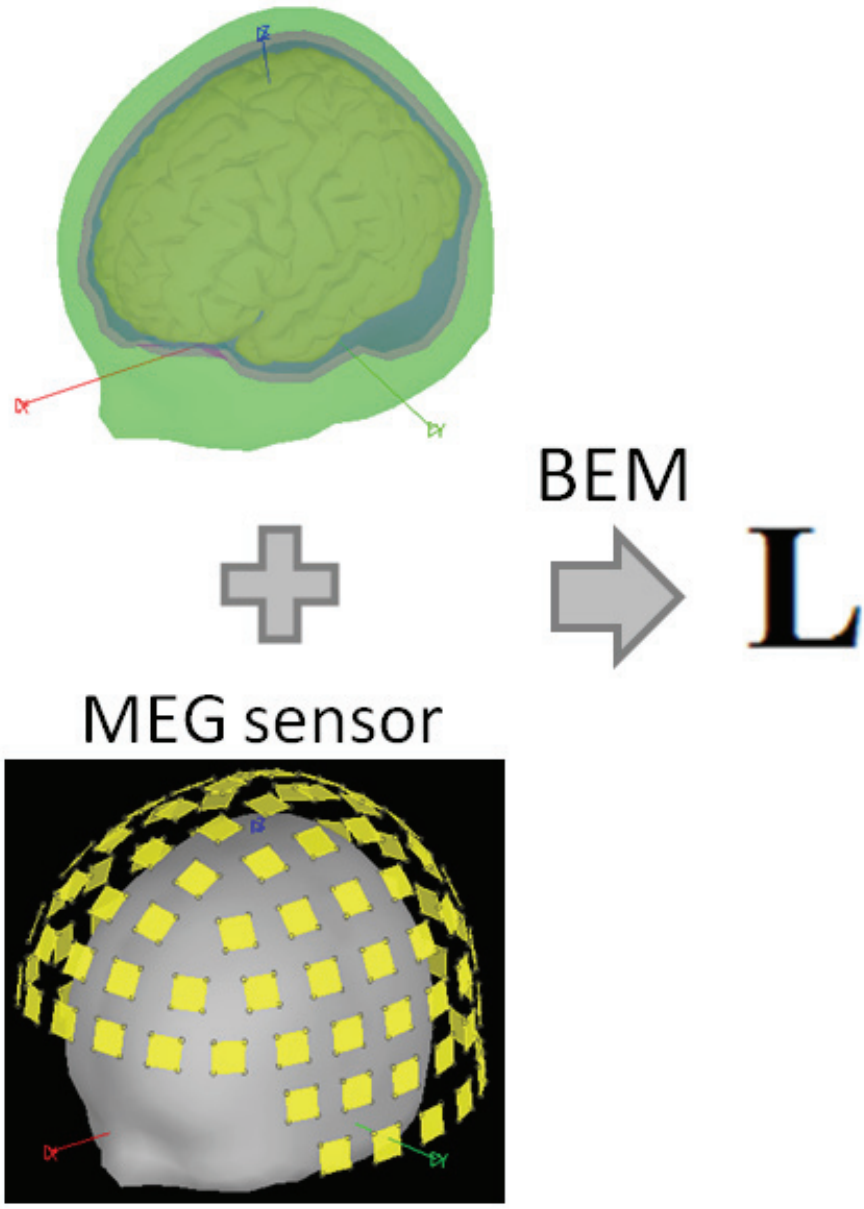

Figure 5-2 Forward model building.

5.3.1 Two Typical Simulations

Two locations indicated by red patches in Figure 5-3 are selected to represent original active sources in the brain. The area of each active source is assumed to be approximately 10 cm^2, and the locations are selected in order to represent the activities within the left superior temporal and precentral gyri. The stable and sharp time series of the active sources are generated according to the following models,

$$\begin{aligned} s_1(t) &= 2 \cdot e^{-\left(\frac{t-200}{60}\right)^2} \cdot \sin[0.004 \cdot \pi \cdot (t-10)] \\ &\quad - 0.8 \cdot e^{-\left(\frac{t-220}{90}\right)^2} \cdot \sin[0.016 \cdot \pi \cdot (t-150)] \\ &\quad (0 < t \le 300\, ms) \end{aligned} \tag{5.12}$$

$$\begin{aligned} s_2(t) &= 0 \ (0 < t \le 200ms, 205 < t \le 300ms) \\ &= A \cdot \sin(0.2 \cdot \pi \cdot t) \ (200 < t \le 205ms) \end{aligned} \tag{5.13}$$

where A is the parameter controlling the amplitude of the time series $s_2(t)$. Since the MEG channel contamination from noise is inevitable, we contaminate the MEG measurements by adding artificial noise for 50 trials. The noise level is set to achieve an average SNR of 15 dB after averaging over all epochs.

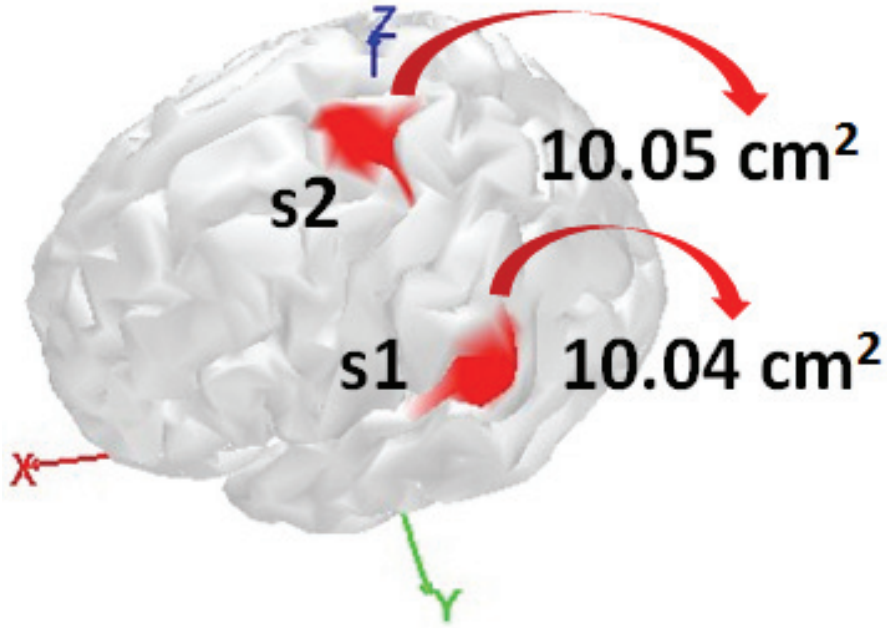

Figure 5-3 Original locations of two active sources.

The sensitivity of the methods to a weak activity s2 ($A = 0.2$) is investigated in Figures 5-4 to 5-6. The original time series of active sources $s_1(t)$ and $s_2(t)$ according to the equations (5.12) and (5.13) at 1 *ms* intervals from 1 to 300 *ms* are shown in red and blue lines in Figure 5-4. The simulated magnetic field recordings calculated by assigning the $s_1(t)$ and $s_2(t)$ to the two activities are also shown in Figure 5-4.

The estimation results obtained by using MN and SDI at 203 *ms* are shown in Figure 5-5, individually. We first use intuitive comparisons to capture relevant features for evaluating the results. As shown in the figure, each image is normalized to its maximum values, such that also smaller details of the distributions remain visible. The color scale was set such that grey color reflects 0 to 5 percent of the maximum intensity within each map. Red color indicates the upper and yellow color indicates the lower intensity range.

Figure 5-5 shows that the source distribution obtained from the MN completely missed the active source s2 at 203ms. The MN generates an active source estimate regardless of the underlying source time series configurations, therefore, the weak sharp signal s2 is easily overlain by the strong signal s1 (at 203 ms, the amplitude of s1 is nearly five times higher than that of s2). The SDI using a decomposition technique overcame this problem, leading to two separate results. The first one being the low-rank component was able to recover correctly the activity s1. The second being the sparse component produced two activities simultaneously and detected correctly the existence of

the activity s2, though the intensity of the estimated s2 is lower than that of the estimated s1.

Moreover, as shown in Figure 5-6, the estimated time series of s1 obtained by MN and the low-rank component are similar to the original time series, indicating that MN and the low-rank component are valid for retrieving the active source with stronger time series. We should note that compared with the estimated time series in the case of the MN, the estimated result in the case of the low-rank component is much smoother, the reason for this is the compensating effect of stabilization from the low-rank component. Since the original time series of s2 is too weak, the estimated time series of s2 are distorted in varying degrees.

These results demonstrate that the SDI can provide almost identical estimate for the strong activity with stable time series, and it can also detect the existence of weak activity with varying time series.

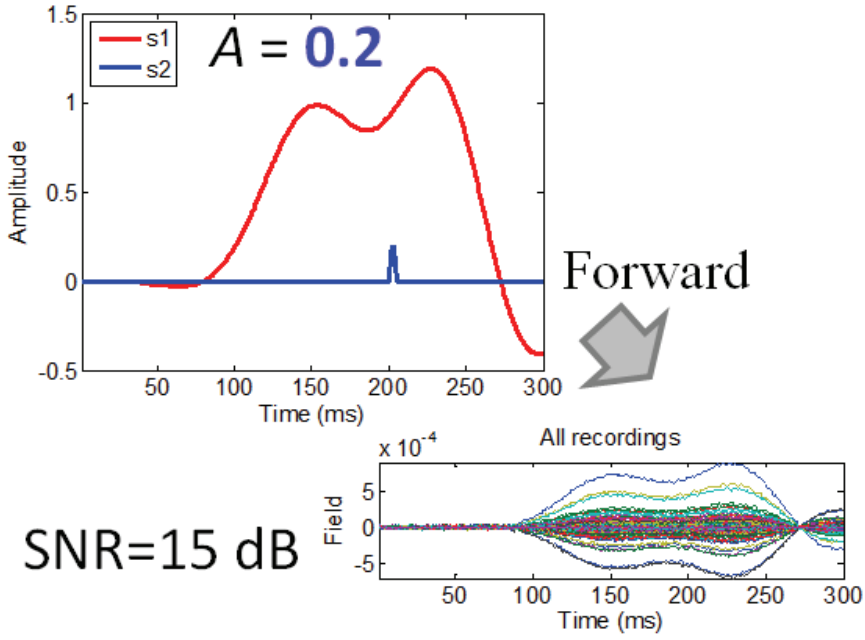

Figure 5-4 Time series of active sources used for simulations and the simulated magnetic field recordings (A=0.2).

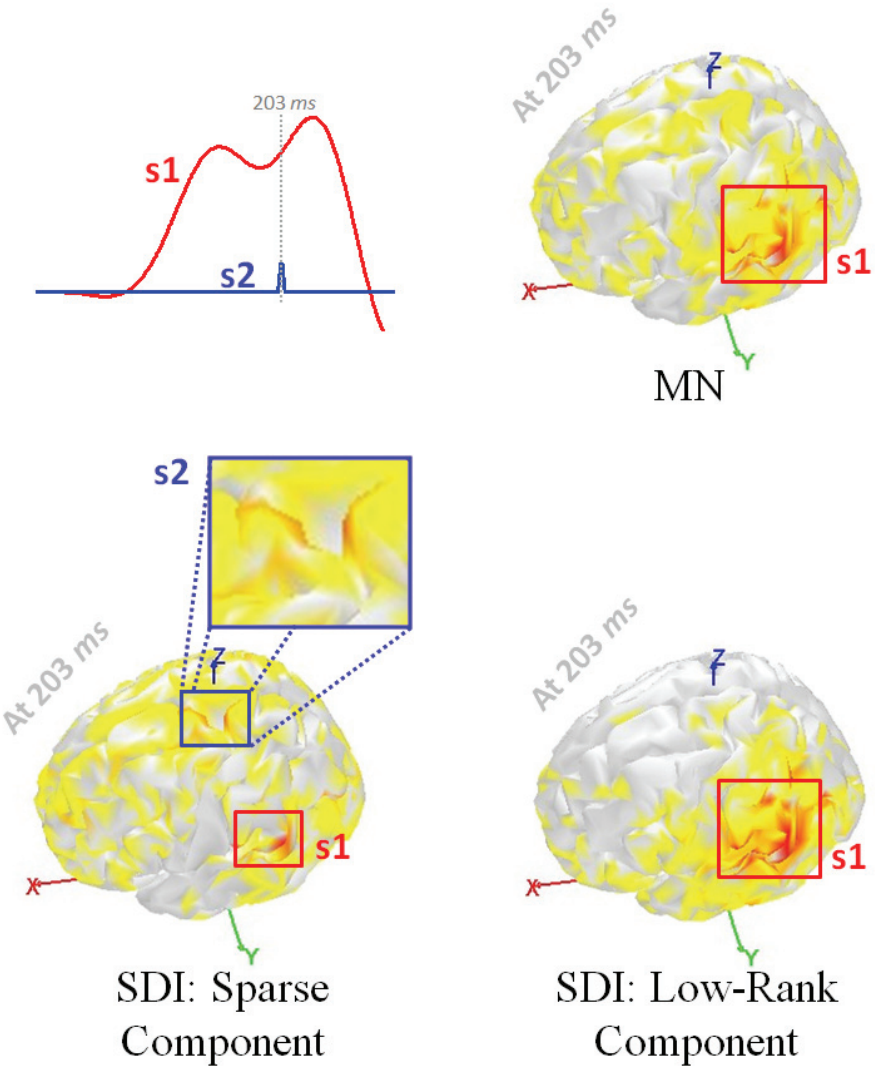

Figure 5-5 Source estimates obtained by MN, SDI: low-rank component and SDI: sparse component at 203ms (A=0.2).

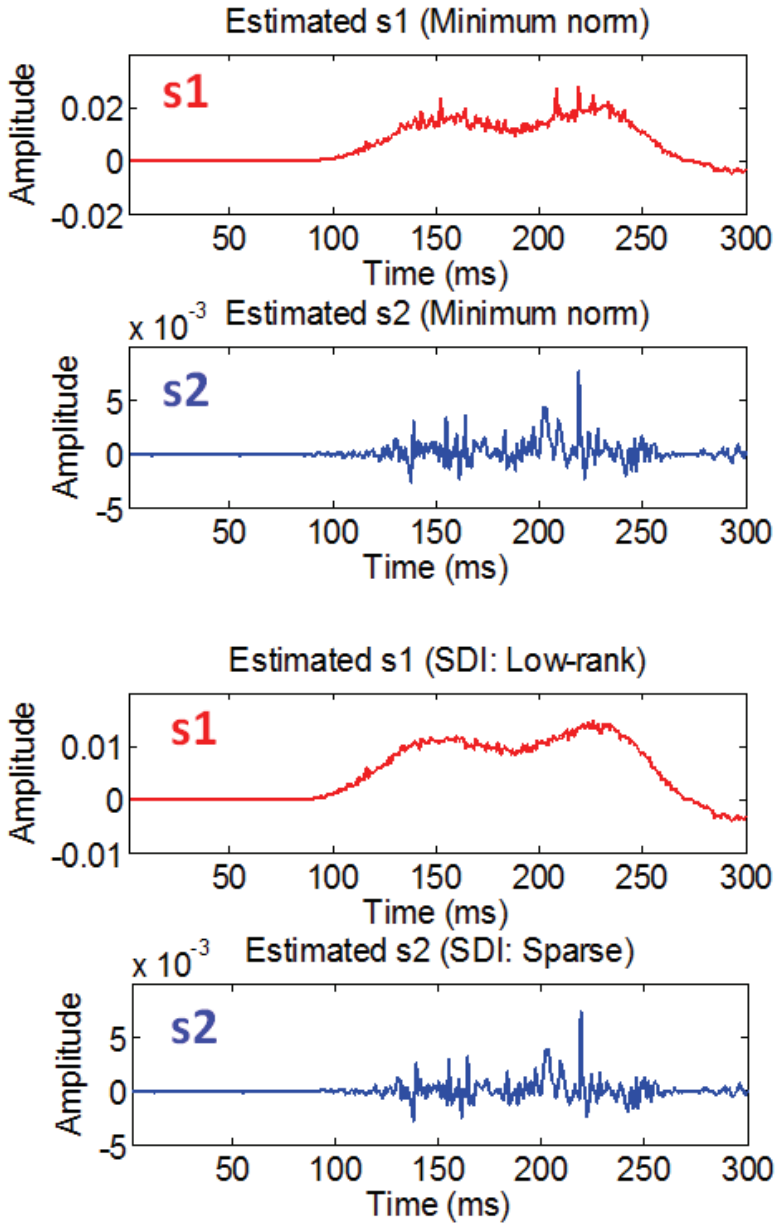

Figure 5-6 Estimated source time series obtained by MN, SDI: sparse component and SDI: low-rank component (A=0.2).

The performance of the estimation methods to a strong activity s2 ($A = 5$) is investigated. The original time series and magnetic recordings are shown in Figure 5-7.

Similar to Figure 5-5, all intensity maps in Figure 5-8 are normalized to their maximum value, so that smaller details can still be identified. Figure 5-8 shows that the source distributions obtained from the MN missed the weak active source s1 at 203ms. However, the SDI recovered the activities of s1 and s2.

As about time series of s2 shown in Figure 5-9, the estimates obtained by MN and the sparse component are almost same as the original s2. In terms of time series of s1, the estimate in the case of MN is contaminated by the strong sharp signal s2 which leads to the unsmooth estimated time series of s1, yet the contamination of strong sharp activity to the estimate of SDI is reduced since the stabilization of the low-rank component.

The results demonstrate that the SDI can provide almost identical estimates for both the weak activity with stable time series and strong activity with varying time series.

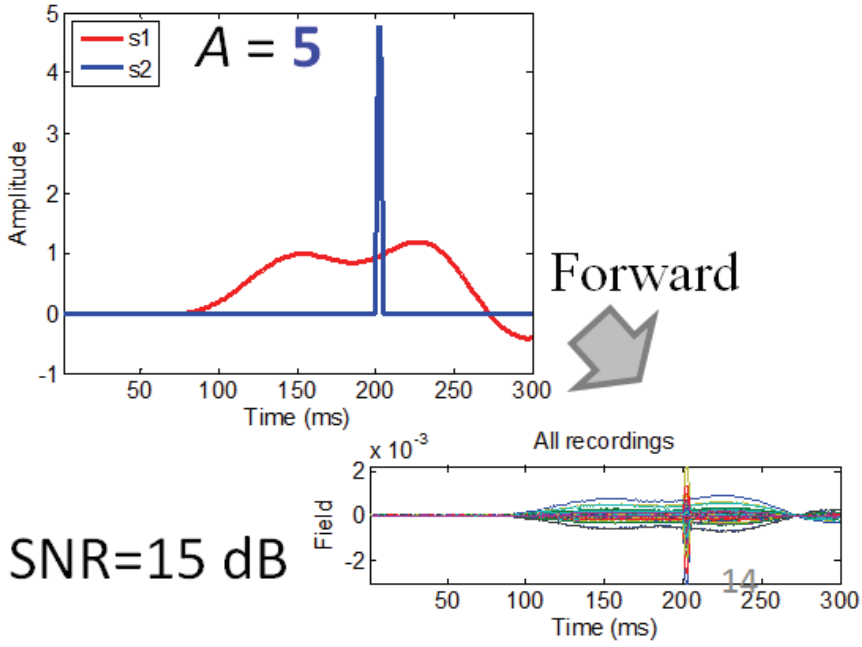

Figure 5-7 Original source time series and the simulated magnetic field recordings (A=5).

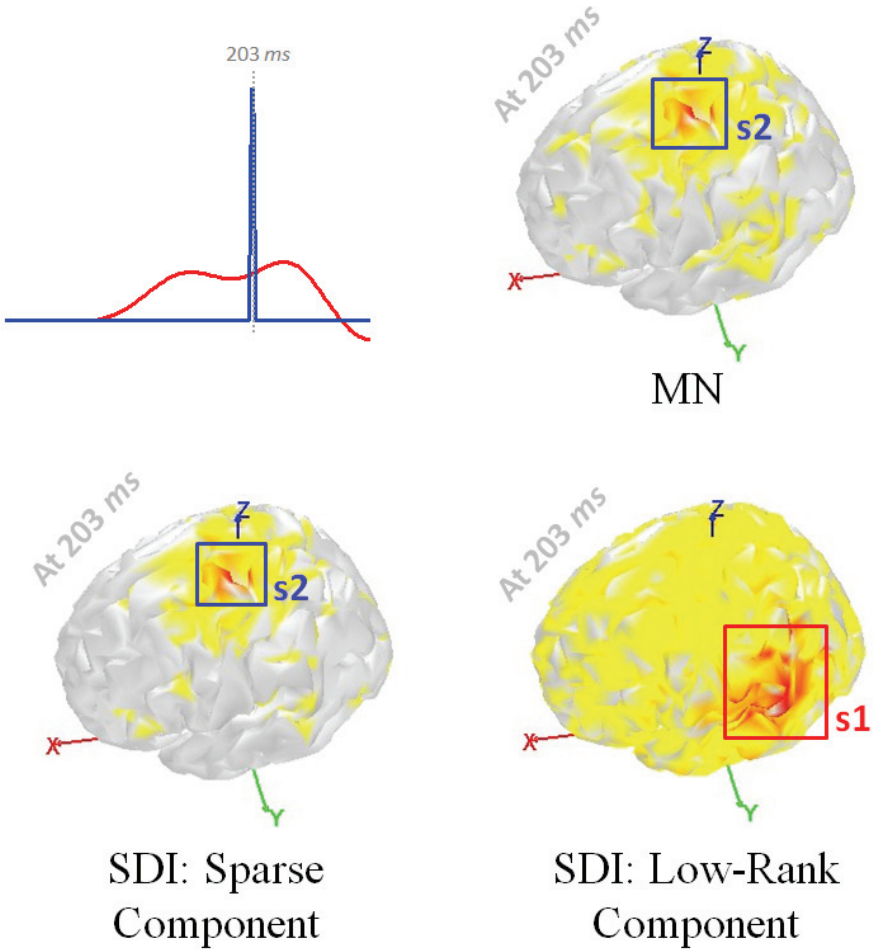

Figure 5-8 Source estimates obtained by MN, SDI: low-rank component and SDI: sparse component at 203ms (A=5).

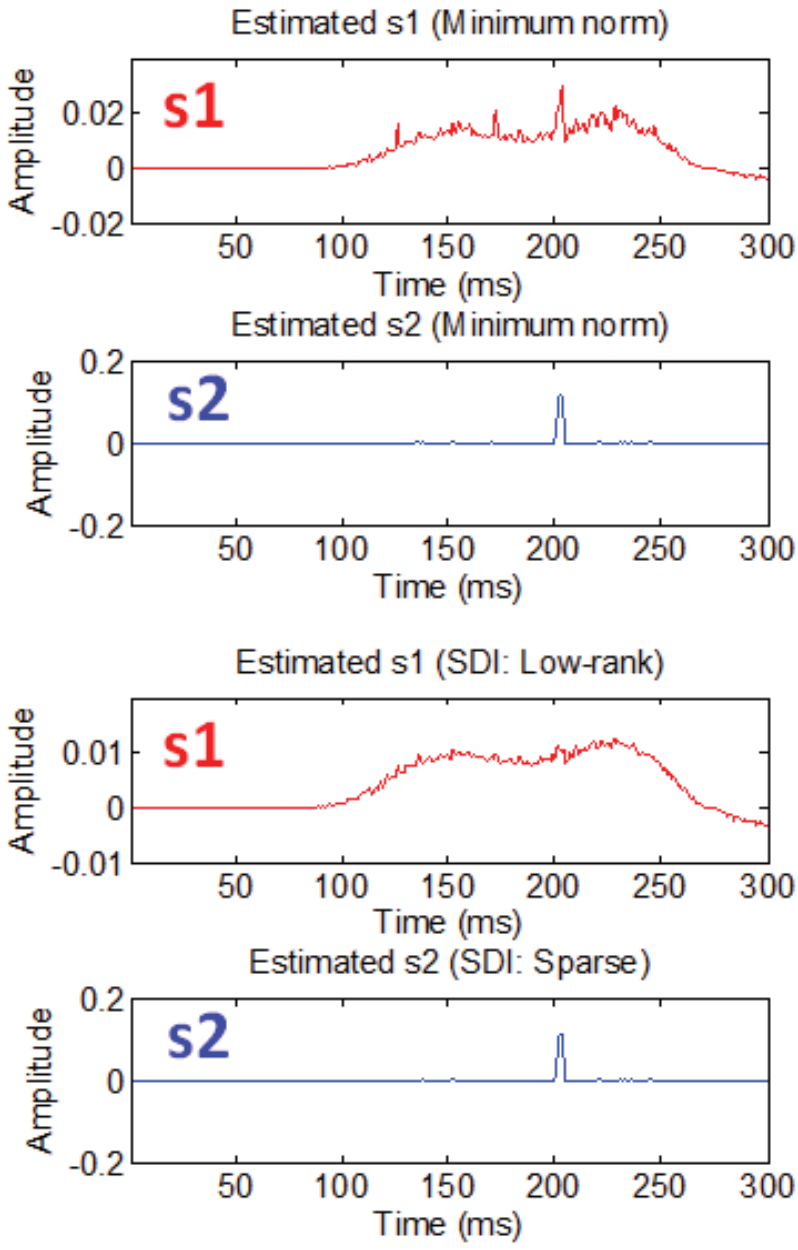

Figure 5-9 Estimated source time series obtained by MN, SDI: sparse component and SDI: low-rank component (A=5).

5.3.2 Simulation of Multi-varying Time Series

In this section, the sensitivity of the estimation methods to the multi-varying time series is investigated. We follow the settings in the previous section. The original locations of two active sources are the same as those represented in the section of 5.3.1. The time series of s1 is generated according to equation (5.14), and the time series of s2 is generated according to equation (5.15).

$$\begin{aligned} s_1(t) = & e^{-\left(\frac{t-200}{60}\right)^2} \cdot \sin[0.004 \cdot \pi \cdot (t-10)] \\ & - 0.4 \cdot e^{-\left(\frac{t-220}{90}\right)^2} \cdot \sin[0.016 \cdot \pi \cdot (t-150)] \\ & (0 < t \le 300\ ms) \end{aligned} \tag{5.14}$$

$$\begin{aligned} s_2(t) = & 0 \ (0 < t \le 120\ ms) \\ = & 1.5 \cdot \sin(0.2 \cdot \pi \cdot t) \ (120 < t \le 125\ ms) \\ = & 0 \ (125 < t \le 150\ ms) \\ = & 0.1 \cdot \sin(0.2 \cdot \pi \cdot t) \ (150 < t \le 155\ ms) \\ = & 0 \ (155 < t \le 170\ ms) \\ = & 0.5 \cdot \sin(0.2 \cdot \pi \cdot t) \ (170 < t \le 175\ ms) \\ = & 0 \ (175 < t \le 200\ ms) \\ = & 0.9 \cdot \sin(0.2 \cdot \pi \cdot t) \ (200 < t \le 205\ ms) \\ = & 0 \ (205 < t \le 230\ ms) \\ = & 2.5 \cdot \sin(0.2 \cdot \pi \cdot t) \ (230 < t \le 235\ ms) \\ = & 0 \ (235 < t \le 250\ ms) \\ = & 0.2 \cdot \sin(0.2 \cdot \pi \cdot t) \ (250 < t \le 255\ ms) \\ = & 0 \ (255 < t \le 300\ ms) \end{aligned} \tag{5.15}$$

The time series of active sources used for simulations and the simulated magnetic field recordings are shown in Figures 5-9 and 5-10, respectively.

The sources and the time series of estimation results are shown in Figures 5-11 and 5-12, respectively. The MN method generated active source estimates regardless of the underlying source time series configurations, therefore, the weak active sources are easily overlain by the strong ones. The source estimates of SDI can flexibly and more accurately reflect the active state of the true simulated sources in the simulation because of the decomposition. The low-rank component of SDI can estimate relatively stationary active source, and the sparse component can product the estimate, which is varying over time. For the integration of the low-rank and sparse components, the SDI result is more similar to the underlying sources than the MN method.

In conclusion, the present simulation studies address the question as to whether the SDI algorithm for neuroelectromagnetic problems improves the estimation of the source signals. The results confirm that using the SDI increases the accuracy of the estimation, and demonstrates that the proposed method is reliable over large underlying source time series configurations, and concludes that the SDI enhances the representation of the original source profiles. In general, the SDI method for measuring neuroelectromagnetic source signals can capture dynamic details and recover the stationary source signal.

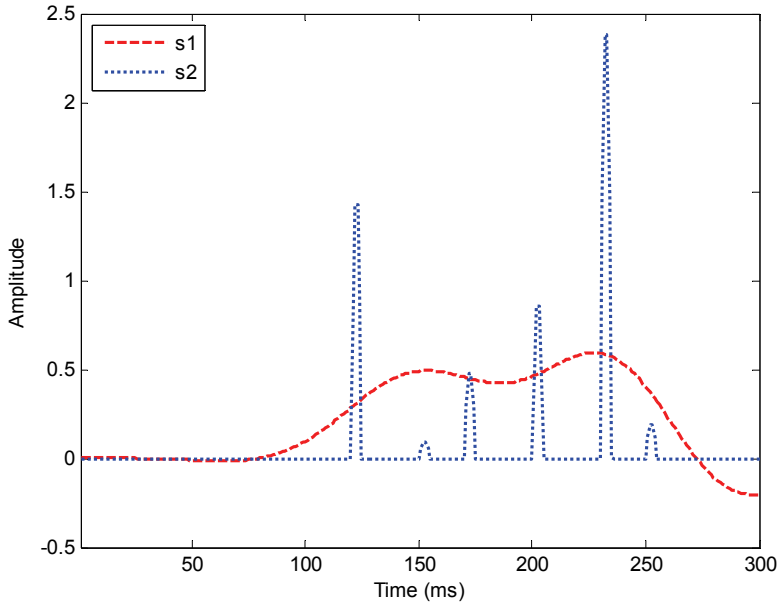

Figure 5-10 Multi-varying time series of active sources used for simulation.

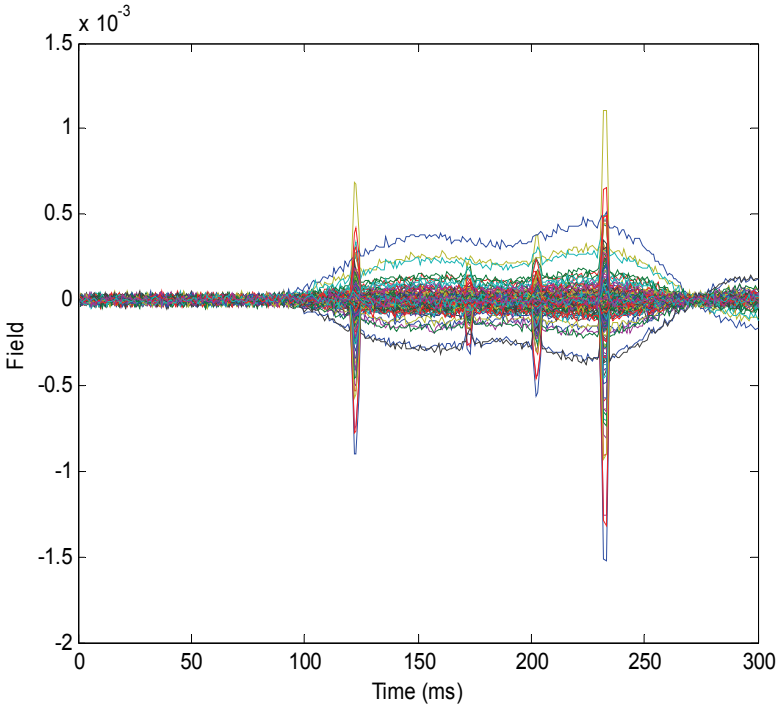

Figure 5-11 Simulated magnetic field recordings.

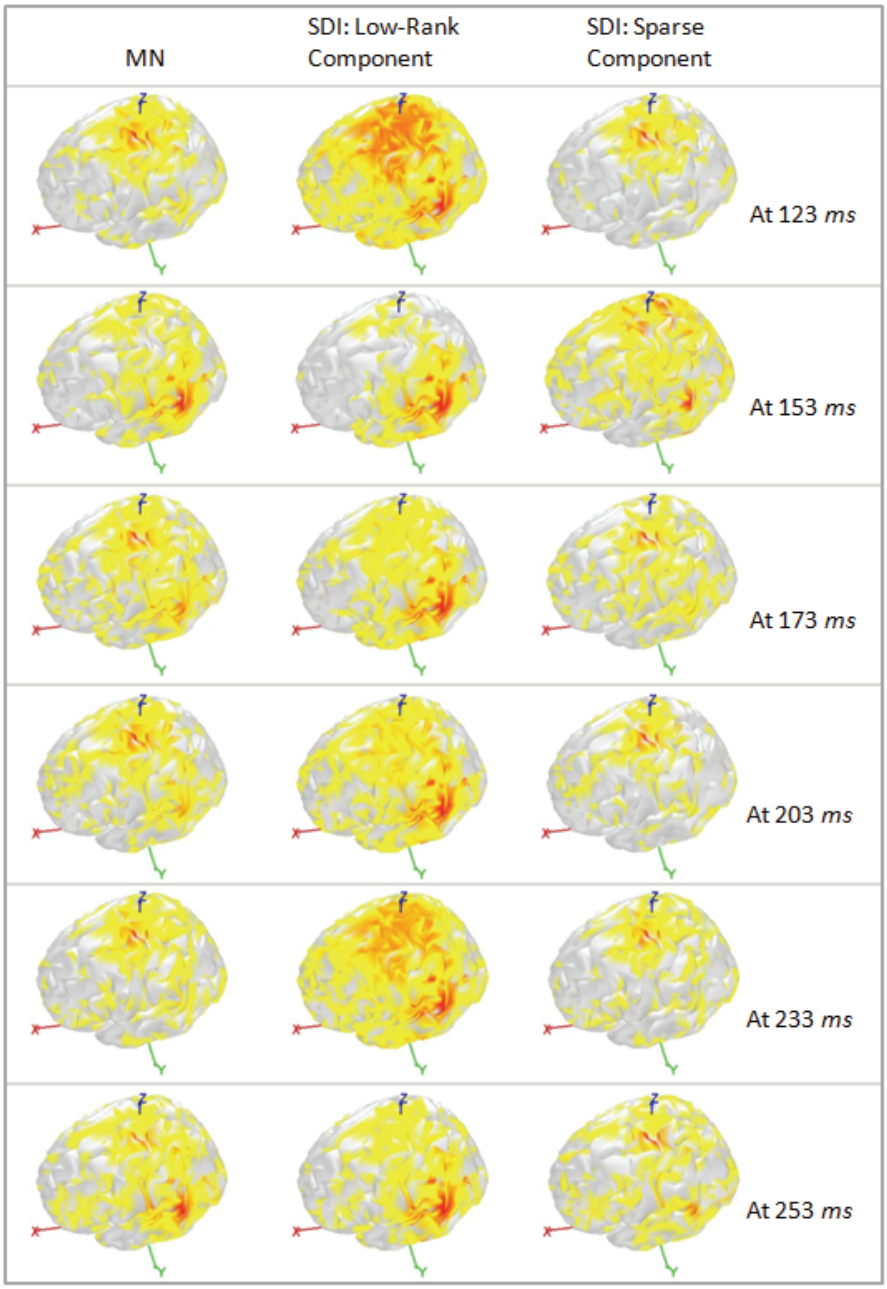

Figure 5-12 Estimation results.

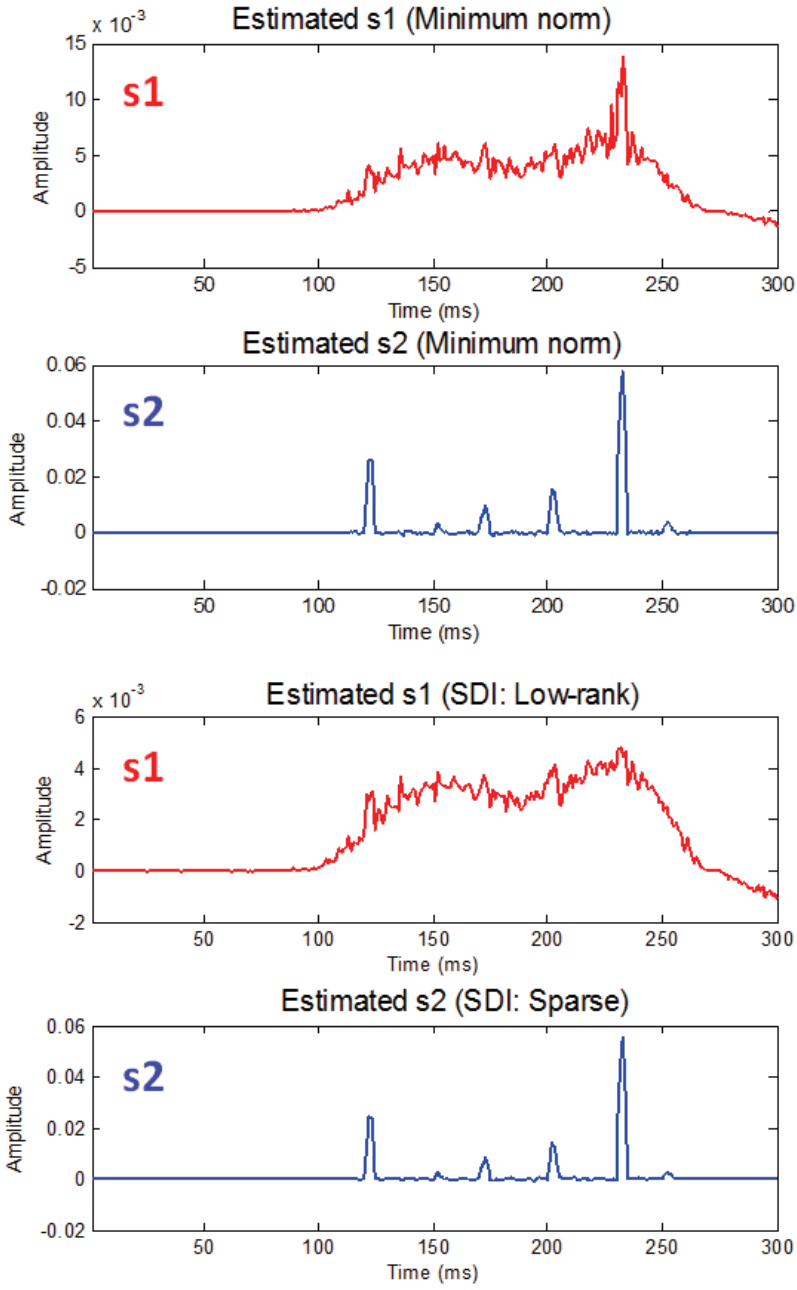

Figure 5-13 Estimated time series of the active sources.

5.4 Application to Practical Measurements

In order to illustrate the performance of the SDI method with practical data, we applies the proposed method to localize the epileptic activity in a patient with medically intractable epilepsy requiring a resective surgery [85]. The patient underwent pre-surgical evaluation was scanned using MR unit with a conventional head gradient coil. The MR images were acquired using a regular T1-weighted sequence for head images. The slice thickness was 1.5 *mm* with acquisition in the sagittal orientation with a matrix size of 256 by 256. Using scanned MR images, BEM models and a cortical source space were extracted using Brainstorm [86]. MEG signals were acquired by the whole-head MEG system (VectorViewTM, Elekta Neuromag Oy, Helsinki, Finland), which consists of 306 channels arranged in triplets of two planar gradiometers (204 channels) and one magnetometer (102 channels). The sampling frequency was 600.615Hz, and the signal was filtered by a band-pass filter in the range of 0.1~200Hz. Since the post-operative MR images of the patient were also acquired, we thus know where the epileptogenic zone is, and therefore, the inverse algorithms can be verified against the exact location of epileptogenic zone. The real epileptic data offers a unique opportunity to verify and compare different inverse algorithms on the same real data [87-94]. As shown in Figure 5-14, we segmented the resection region from the post-operative MR images and co-registered the resection region to the cortex surface segmented by pre-operative MR images using Brainstorm software [86]. Figure 5-15 schematically illustrates the overall procedure of localizing epileptic activity

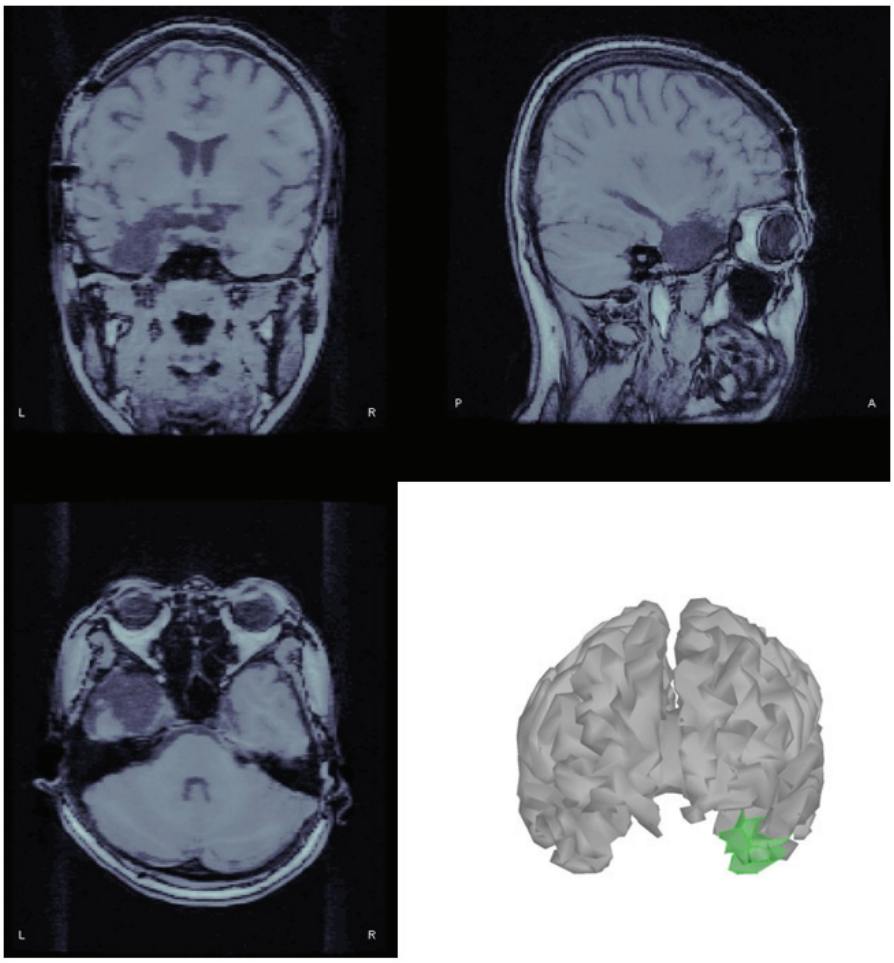

Figure 5-14 Resection region.

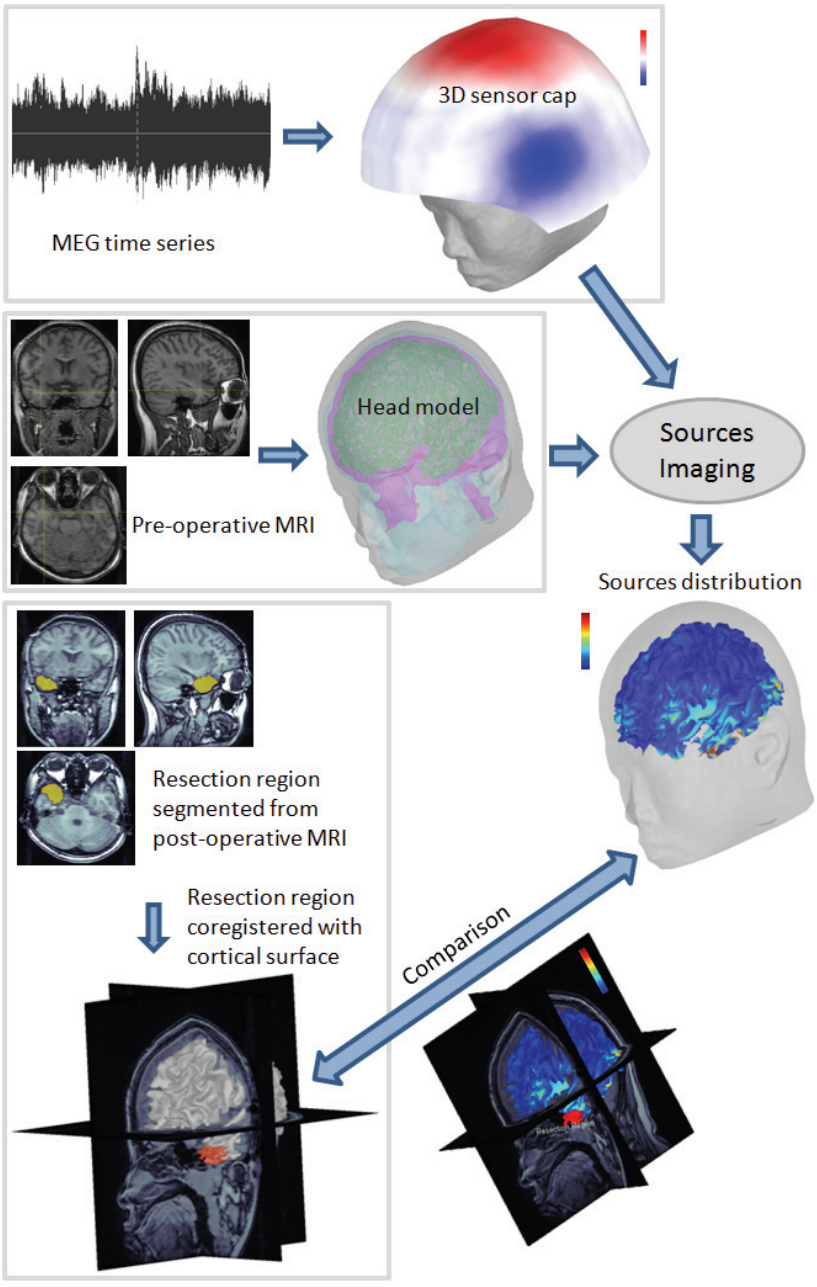

Figure 5-15 Overall procedure of localizing epileptic activity.

We take into account two assessment criteria using the surgical resection region on the cortex surface as a reference to quantitatively evaluate the performance of the source estimation. The first criterion is localization error (LE), which is determined as the shortest distance from the source location with maximum source strength to the boundary of the resection region, to assess the performance of localization. If the location with the maximum value is localized within the resection region, the localization error is assigned the value zero [88, 91].

We use another criterion denoted as degree of focalization (DF) to quantify the consistency of the estimated source distribution with resection region [95]. DF is defined as the estimated source energy contained in the reference source space (i.e., the surgical resection region in this study) divided by the overall source energy, which is the source energy in the whole source space. This criterion can be applied in the subject study because of the explicit resection region [96]. Thus, the larger the DF value the more accurate source distribution that the estimation method can obtain [13, 97].

In epilepsy studies, the accuracy of source estimation is variable across different time points of an interictal spike, unfortunately, the relationship is not yet well understood [88]. Since all the methods get their best DF values at the 223th sample point shown in Figure 5-16, we investigates source estimation of interictal spike activity at this point.

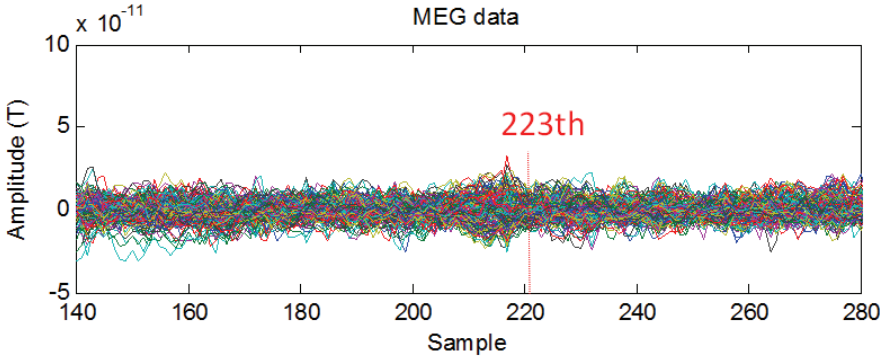

Figure 5-16 MEG waveform of the epilepsy patient.

We first use intuitive criterion to capture relevant features for evaluating the spatial resolutions. As shown in Figure 5-17, the results estimated by MN and SDI are shown under the same conditions.

The figure shows that the source distribution obtained from MN method is discontinuous and contains several local maxima (spurious sources) at a considerable distance from the true source location. This reflects the MN bias in epileptic activity localization. If such a result was encountered in a real experiment, without prior knowledge of the true number of sources, the location of the unknown epileptic activity would not be found successfully.

However, the SDI sparse component seems to be more effective, it obtains more focused source distribution with less spurious sources, and the epileptic activity is well localized. This result also exactly confirms that the pattern of epileptic activity is sparse. The result of SDI low-rank component is similar to that of MN because of the sparse pattern of epileptic activity.

The LE and DF results are presented in the top left corner of Figure 5-17 to quantitatively compare the performance of the estimations. All the methods produce the location with the maximum value in the resection region because all the LE results are 0. Since SDI sparse component gets the largest the DF value, the SDI sparse obtains the most accurate source distribution.

The intuitive and quantitative comparisons suggest that the proposed SDI enhances the estimation accuracy.

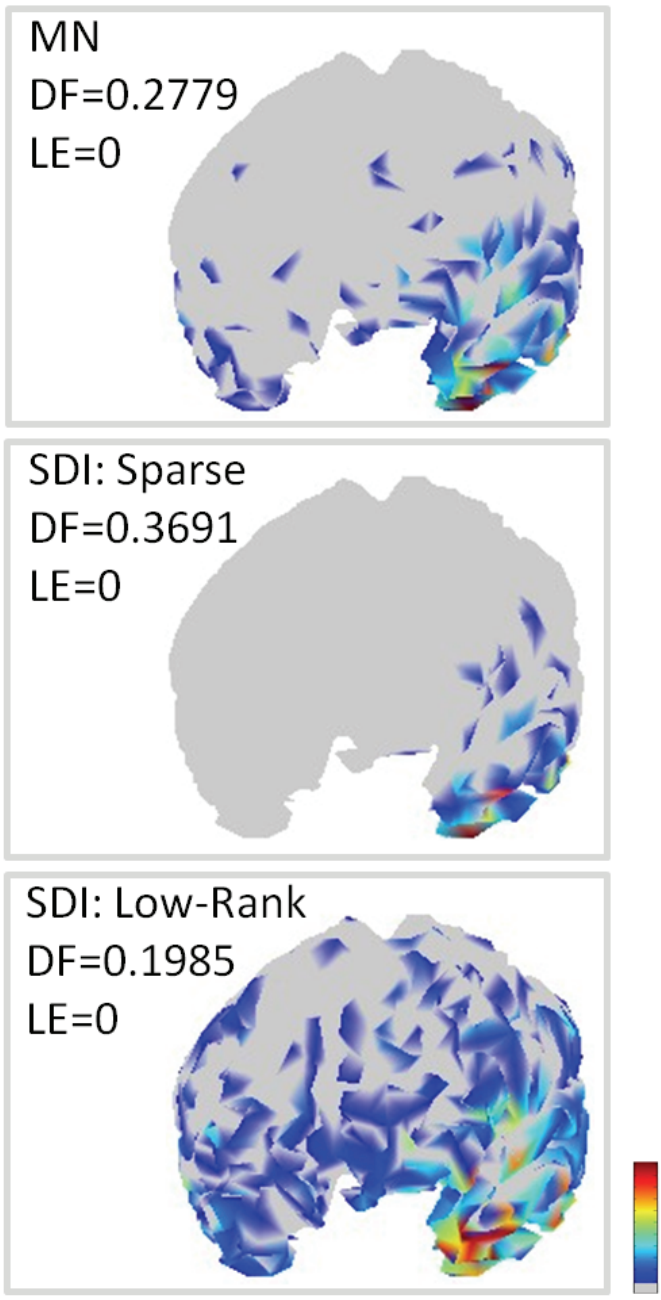

Figure 5-17 Estimated results of epileptic activity.

5.5 Noise Suppression in MEG Measurement for Improving Neuroelectromagnetic Source Estimation

MEG uses an array of sensors positioned over the whole head that are extremely sensitive to the minuscule changes in the magnetic fields produced by the electrical activity in the brain. Recently, the development of whole-head MEG sensor arrays and of methods for estimation of neuroelectromagnetic sources from the MEG measurement has been remarkable. Nevertheless, all existing methods for neuroelectromagnetic source estimation are hampered by the many sources of noise present in the outside measurement [98-100]. Much research has been performed over the years on noise suppression in neuroelectromagnetic measurement. For example, principal component analysis (PCA) has been used for data processing, analysis and noise reduction. However, many research works have been proposed to address the brittleness of the classical PCA with respect to outliers and gross corruption in the literature over several decades [80]. In this chapter, a novel noise suppression method, based on SDI technique, is presented and applied to the estimation of neuroelectromagnetic field in source space for the first time. The proposed method gives a constrained optimization of MEG electromagnetic domain transformations such that the matrix of transformed MEG measurement can be decomposed as the sum of a sparse matrix of noise and a low-rank matrix of denoised data. The decomposition is a unique feature of the proposed method which not only can suppress the noise, but also can preserve the information about the underlying neuroelectromagnetic sources. We verified the efficacy of the proposed

method with a number of simulations under different configurations. Our results indicated that the performance of source estimation is significantly improved.

5.5.1 Method

In MEG, the electromagnetic measurement is a superposition of information component and noise component, therefore, the component of MEG data has low intrinsic dimensionality, i.e., it lies on some low-dimensional subspace, or it is sparse. Mathematically, this means the measured electromagnetic field $\mathbf{Y}$ can be decomposed into a low-rank matrix and a sparse matrix such that $\mathbf{Y} = \mathbf{Y}_L + \mathbf{Y}_S$, where $\mathbf{Y}_L$ has low rank and $\mathbf{Y}_S$ is sparse. Obviously, the component $\mathbf{Y}_S$ carries the information of the neuroelectromagnetic source signal, and the component $\mathbf{Y}_S$ carries the noise. Given these properties, we present in this work a novel method based on SDI to suppress the noise in MEG data. The proposed method is defined as the following constrained optimization of a cost function,

$$\min_{\mathbf{Y}_L,\mathbf{Y}_S} \|\mathbf{Y}_L\|_* + \gamma \|\mathbf{Y}_S\|_1 \ \textit{subject to} \ \ \mathbf{Y} = \mathbf{Y}_L + \mathbf{Y}_S \qquad (5.16)$$

For the problem of neuroelectromagnetic source estimation, we do not know the low-dimensional subspace of $\mathbf{Y}_L$ as well as the locations and number of

the nonzero entries of $\mathbf{Y}_S$. Figure 5-18 shows the overall procedure for solving the SDI-based noise suppression in MEG measurement.

Initialization:

$$k=0$$

$$\mathbf{Y}_{S_0}=0$$

$$\mathbf{Y}_{L_0}=0$$

$$\mu_0=\frac{1.25}{\|\text{sign}(\mathbf{Y})\|_2}$$

$$\gamma=\frac{1}{\sqrt{\max(M,T)}}$$

$$\mathbf{L}_{A_0}=\frac{\text{sign}(\mathbf{Y})}{\max\left(\|\text{sign}(\mathbf{Y})\|_2,\gamma^{-1}\|\text{sign}(\mathbf{Y})\|_\infty\right)}$$

where $\text{sign}(\cdot)$ is the signum function.

Iteration:

$$\left(U,S,V^T\right)=\text{svd}\left(\mathbf{Y}-\mathbf{Y}_{S_k}+\mu_k^{-1}\mathbf{L}_{A_k}\right)$$

$$\arg\min_{\mathbf{Y}_{L_{k+1}}} L(\mathbf{Y}_{L_{k+1}},\mathbf{Y}_{S_k},\mathbf{L}_{A_k},\mu_k)=U\left(\Gamma_{\mu_k^{-1}}[S]\right)V^T$$

$$\arg\min_{\mathbf{Y}_{S_{k+1}}} L(\mathbf{Y}_{L_{k+1}},\mathbf{Y}_{S_{k+1}},\mathbf{L}_{A_k},\mu_k)=$$

$$\Gamma_{\lambda\mu_k^{-1}}\left[\mathbf{Y}-\mathbf{Y}_{L_k}+\mu_k^{-1}\mathbf{L}_{A_k}\right]$$

$$\mathbf{L}_{A_{k+1}}=\mathbf{L}_{A_k}+\mu_k\left(\mathbf{Y}-\mathbf{Y}_{L_{k+1}}-\mathbf{Y}_{S_{k+1}}\right)$$

$$\mu_{k+1}=1.5\mu_k$$

$$k=k+1$$

$$\text{where } \Gamma_\varepsilon[x]=\begin{cases}x-\varepsilon,\text{if } x>\varepsilon\\ x+\varepsilon,\text{if } x<-\varepsilon\\ 0,\text{otherwise}\end{cases}$$

Terminate if no improvements in $\mathbf{Y}_S$ and $\mathbf{Y}_L$.

Figure 5-18 The overall procedure for solving the SDI-based noise suppression.

5.5.2 Simulations and Results

The system configuration for the simulation is shown in Fig. 2(b). The BEM model with 3502 source dipoles is applied for the forward calculation of MEG measurements. Two regions indicated by red patches in Fig. 2(a) are selected to represent original neuroelectromagnetic active sources in the brain. The time series of two activies are also shown in Fig. 2(a). The MEG measurement noise is set to an SNR of -5 dB, and Fig. 2(b) shows the simulated electromagnetic field measurements.

We first use intuitive comparisons to capture relevant feature for evaluating the spatial resolutions. Figures 5-19(c) and (d) show the neuroelectromagnetic source distributions at 227 *ms* estimated by the traditional and proposed methods under the SNR of -5 dB. Figure 5-19(c) shows that the source distributions obtained from the traditional method are discontinuous and contain several spurious sources around the true activity regions. This reflects the weakness of the traditional method under the high noise condition. However, the proposed method seems to be more effective. Figure 5-19(d) shows that the proposed method obtains more focused source distributions with less spurious sources, and the true activities are well estimated. The intuitive comparisons suggest that the proposed method enhances the estimation accuracy.

Furthermore, the DF is used to quantify the consistency of the estimated source distributions with the regions of true activities. According to definition mentioned above, the larger the DF value the more accurate source

distribution that the method can obtain. The application of the proposed method resulted in significant performance improvements over the traditional method, with DF improvement of 3.30% compared to the traditional method. The result demonstrates the effectiveness of the proposed method for enhanced the focal characteristic.

Since the MEG measurement is severely contaminated by the high level noise, the estimated time series of two activities at the regions of interest are unsmooth. However, we should note that compared with the estimated time series in the case of the traditional method, the estimated results in the case of the proposed method are much smoother, the reason for this is the compensating effect of stabilization from the low-rank constraint. Moreover, The CC of the original source time series and the estimated one is presented to quantitatively compare the performance of the traditional and proposed methods. The quantitative improvements are also observed that the CCs of s1 and s2 are improved by 0.0314 and 0.0478 respectively. All of those demonstrates the ability of the proposed method in suppressing noise while preserving the information of neuroelectromagnetic source signals.

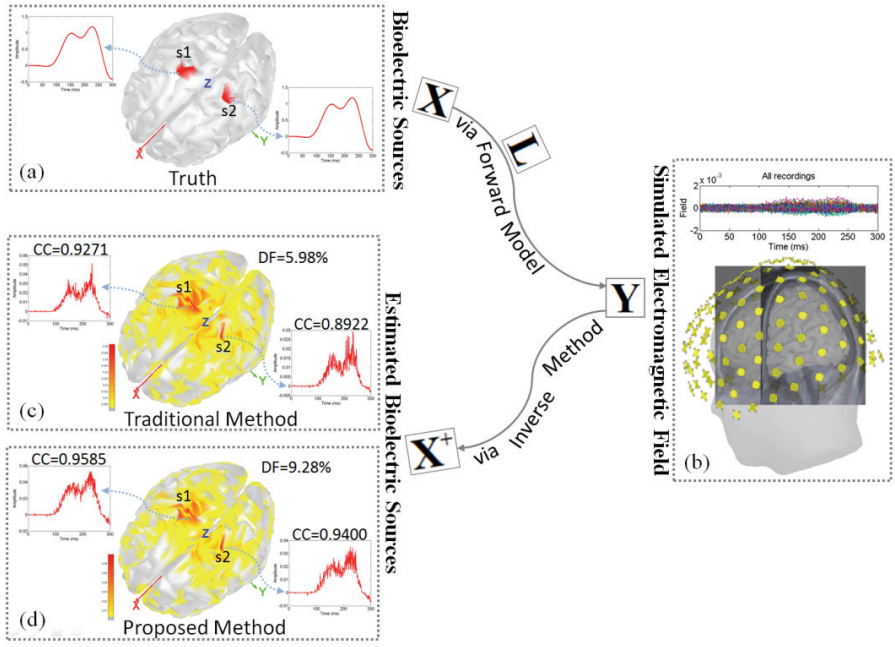

Figure 5-19 Simulation setups and results. (a) The locations and time series of the active sources. (b) The simulated electromagnetic field measurements under -5 dB SNR. (c) The results (estimated source distributions at 227 *ms* and estimated source time series) via traditional method. (d) The results via proposed method.

Table 11 shows the comparison between the DF values obtained by traditional method and proposed method under different noise conditions. Table 12 shows the comparison between the CC values of the true and estimated time series of s1 and s2 obtained by two different methods. As shown in Tables 11 and 12, much of noise in MEG measurements has been suppressed by the proposed method, yielding more accurate estimates (larger DF and CC values), compared with those from traditional method.

In this study, we demonstrated the efficacy of a sparse and low-rank constrained optimization to suppress the noise in MEG measurement for improving neuroelectromagnetic source estimation. The decomposition of MEG data into a sparse matrix of noise and a low-rank matrix of underlying bio-electromagnetic information is a unique feature of the proposed method which not only can suppress the noise, but also can preserve the underlying information about the neuroelectromagnetic sources. In general, the application of this technique to the processing of neuroelectromagnetic source imaging significantly improved the estimate quality. The results suggest that the proposed method could be a powerful tool for many future neuroelectromagnetic applications.

Table 11 DFs of the estimated source distributions

		5 dB	0 dB	-5 dB	-10 dB	-15 dB
at the time point 227 ms	Traditional Method	11.25%	9.75%	5.98%	3.82%	2.10%
	Proposed Method	13.85%	10.91%	9.28%	6.02%	3.72%
average result of all time points	Traditional Method	6.27%	4.65%	3.16%	1.95%	1.13%
	Proposed Method	8.49%	6.90%	5.32%	3.67%	2.32%

Table 12 CCs of the true and estimated time series

		5 dB	0 dB	-5 dB	-10 dB	-15 dB
s1	Traditional Method	0.9804	0.9528	0.9271	0.8790	0.6931
	Proposed Method	0.9914	0.9798	0.9585	0.8898	0.8040
s2	Traditional Method	0.9588	0.9244	0.8922	0.8242	0.6804
	Proposed Method	0.9780	0.9681	0.9400	0.8763	0.7551

6 Conclusion

In this thesis, the techniques to enhance estimating accuracy of neuroelectromagnetic sources were studied. The subspace decomposition imaging and inverse algorithms, which can overcome several problems of the conventional approaches, were proposed. The methods presented in this thesis employ the biologic characteristics to constrain the neuroelectromagnetic source signal imaging. The constraint effectively integrates the spatial and temporal information and improves the resolution of the source estimation. Results reported in this thesis suggest that it is possible to obtain real improvement in the details of the estimated distributed sources by implementing the proposed approaches. Based on the simulations and practical application, the general efficacy and contribution of this thesis can be confirmed by the following observations.

First, the abilities of two different methods, the GCV and the L-curve, in order to determine the proper degree of regularization have been simulated for a range of MEG estimation conditions in conjunction with brain perturbations and measurement noise. Even though the cases investigated in this thesis demonstrate that there is no absolutely better method, the results presented may become useful guidelines for the correct choice of the regularization parameter determination method used in real world neuroelectromagnetic source imaging.

Second, we focused on inverse algorithms and examined their strengths and weaknesses in estimating deep space activities, in the presence of correlation, and compared the performance of the spatial filter, the conventional and proposed linear estimations under such conditions. Based on simulations carried out, we demonstrated that the ability to estimate such activities depends on the weighting matrix and the proposed method performed significantly better than the conventional linear estimations and spatial filter. The linear inverse operator proposed in this thesis employed the suggested correlation weighting matrix to enhance the representation for profiles of correlated neuroelectromagnetic activities located in the deep source space. We relied on realistic simulations to show that the proposed method effectively enlarged the property of the deep sources, provided more detailed information for the source localization, and then improved the final estimation, therefore is physically more reasonable. In this study, the use of the correlation to build the weighting matrix is just an ideal starting point. In fact, revealing the relationship of sources is an active topic in the research community, many methods have been proposed, such as, correlation coefficient, synchrony, coherence, Granger causality, etc. Therefore, reasonable use of more sophisticated relationship analysis methods is required for a more efficient and broad application of the proposed inverse technique in estimating the correlated deep active sources. This also provides a motivator for future works.

Third, we described the inverse algorithms to reconstruct source connectivity network from MEG data, and compared the effectiveness of the linear estimation, the spatial filter and the proposed approach, on the metrics of the

source series, the connectivity magnitude and norm error. We confirmed that the noise effect for the linear estimation is direct, while the effect for the spatial filtering technique is indirect. Moreover, the linear estimation is advantageous for the connectivity reconstruction of high quality outside measurement data, while, the benefit for the case of spatial filter is the low SNR environment. This thesis also proposed a modified spatial filtering technique to improve the neuroelectromagnetic source connectivity network reconstruction. The results indicated that the proposed approach prevents the inclusion of the spurious connectivity, decreases the error fluctuation, improves the reconstruction accuracy, enhances the robustness with respect to the inevitable noise, therefore, represents the profiles of original source connectivity network precisely.

Fourth, the decomposition of source signal into low-rank and sparse components is a unique feature of the SDI method which not only can capture dynamic details in the source space that would sometimes be too weak to be recognized by the conventional method, but also can recover the stationary source signal contaminated by large brain perturbation. The source estimates of SDI can flexibly reflect the active state of the underlying source. In general, SDI demonstrates qualitatively the benefit of using the decomposition technique in analysis of neuroelectromagnetic inverse problems. The proposed SDI is not only tied to a particular inverse algorithm for source estimation, in other words, one is free to choose the type of inverse algorithm, i.e., algorithms such as wMNE, spatial filter, LORETA, dSPM, etc., are valuable candidates for the SDI approach. In the implementation of SDI presented here, we use the least constraint method, i.e., MN linear estimation. In principal,

using other inverse algorithms in SDI is equivalent to the method demonstrated in this thesis.

Fifth, MEG is a promising technology, which could be used in a variety of biomedical applications, however, MEG electromagnetic measurement is usually degraded by noise. The SDI-based noise suppression method gives a constrained optimization of MEG electromagnetic domain transformations such that the matrix of transformed MEG measurement can be decomposed as the sum of a sparse matrix of noise and a low-rank matrix of denoised data. Applying the proposed method to a number of simulations showed significant improvement of the result accuracy.

Finally, it should be pointed out that, revealing biophysical phenomena with inverse techniques is a hot topic in the neuroscience community, therefore, after reasonable interpretation of well-known and acknowledged biophysical characteristics, we may also build other sophisticated approaches for analysis of neuroelectromagnetic problems in the future.

References

[1] M. Hamalainen, *et al.*, "Magnetoencephalography - Theory, instrumentation, and applications to noninvasive studies of the working human brain," *Reviews of Modern Physics,* vol. 65, pp. 413-497, Apr 1993.

[2] W. T. Chang, *et al.*, "Spatially sparse source cluster modeling by compressive neuromagnetic tomography," *Neuroimage,* vol. 53, pp. 146-160, Oct 15 2010.

[3] P. Xu, *et al.*, "Neuroelectric source imaging using 3SCO: A space coding algorithm based on particle swarm optimization and l0 norm constraint," *Neuroimage,* vol. 51, pp. 183-205, May 15 2010.

[4] M. Woolrich, *et al.*, "MEG beamforming using Bayesian PCA for adaptive data covariance matrix regularization," *Neuroimage,* vol. 57, pp. 1466-1479, Aug 15 2011.

[5] C. M. Michel, *et al.*, "EEG source imaging," *Clinical Neurophysiology,* vol. 115, pp. 2195-2222, Oct 2004.

[6] C. H. Im, *et al.*, "Precise estimation of main electrical sources using anatomically constrained area source (ACAS) localization," *Ieee Transactions on Magnetics,* vol. 43, pp. 1713-1716, Apr 2007.

[7] K. Sekihara, *et al.*, "Performance of an MEG adaptive-beamformer technique in the presence of correlated neural activities: effects on signal intensity and time-course estimates," *Ieee Transactions on Biomedical Engineering,* vol. 49, pp. 1534-1546, Dec 2002.

[8] C. H. Im, *et al.*, "An EEG-based real-time cortical rhythmic activity monitoring system," *Physiological Measurement,* vol. 28, pp. 1101-1113, Sep 2007.

[9] H. J. Hwang, *et al.*, "An EEG-based real-time cortical functional connectivity imaging system," *Medical & Biological Engineering & Computing,* vol. 49, pp. 985-995, Sep 2011.

[10] R. Grech, *et al.*, "Review on solving the inverse problem in EEG source analysis," *Journal of Neuroengineering and Rehabilitation,* vol. 5, Nov 7 2008.

[11] B. D. VanVeen, *et al.*, "Localization of brain electrical activity via linearly constrained minimum variance spatial filtering," *Ieee Transactions on Biomedical Engineering,* vol. 44, pp. 867-880, Sep 1997.

[12] S. Baillet, *et al.*, "Electromagnetic brain mapping," *Ieee Signal Processing Magazine,* vol. 18, pp. 14-30, Nov 2001.

[13] C. Grova, *et al.*, "Evaluation of EEG localization methods using realistic simulations of interictal spikes," *Neuroimage,* vol. 29, pp. 734-753, Feb 1 2006.

[14] O. Hauk, "Keep it simple: A case for using classical minimum norm estimation in the analysis of EEG and MEG data," *Neuroimage,* vol. 21, pp. 1612-1621, Apr 2004.

[15] F. H. Lin, *et al.*, "Assessing and improving the spatial accuracy in MEG source localization by depth-weighted minimum-norm estimates," *Neuroimage,* vol. 31, pp. 160-171, May 15 2006.

[16] A. Bolstad, *et al.*, "Space-time event sparse penalization for magneto-/electroencephalography," *Neuroimage,* vol. 46, pp. 1066-1081, Jul 15 2009.

[17] O. Hauk, *et al.*, "Comparison of noise-normalized minimum norm estimates for MEG analysis using multiple resolution metrics," *Neuroimage,* vol. 54, pp. 1966-1974, Feb 1 2011.

[18] D. S. Barth, *et al.*, "Neuromagnetic localization of epileptiform spike activity in the human-brain," *Science,* vol. 218, pp. 891-894, 1982.

[19] B. A. Olshausen and D. J. Field, "Emergence of simple-cell receptive field properties by learning a sparse code for natural images," *Nature,* vol. 381, pp. 607-609, Jun 13 1996.

[20] W. M. Ou, *et al.*, "A distributed spatio-temporal EEG/MEG inverse solver," *Neuroimage,* vol. 44, pp. 932-946, Feb 1 2009.

[21] I. F. Gorodnitsky, *et al.*, "Neuromagnetic source imaging with focuss - A recursive weighted minimum norm algorithm," *Electroencephalography and Clinical Neurophysiology,* vol. 95, pp. 231-251, Oct 1995.

[22] I. F. Gorodnitsky and B. D. Rao, "Sparse signal reconstruction from limited data using FOCUSS: A re-weighted minimum norm algorithm," *Ieee Transactions on Signal Processing,* vol. 45, pp. 600-616, Mar 1997.

[23] P. Xu, *et al.*, "Lp norm iterative sparse solution for EEG source localization," *Ieee Transactions on Biomedical Engineering,* vol. 54, pp. 400-409, Mar 2007.

[24] K. Matsuura and Y. Okabe, "Selective minimum-norm solution of the biomagnetic inverse problem," *Ieee Transactions on Biomedical Engineering,* vol. 42, pp. 608-615, Jun 1995.

[25] K. Uutela, *et al.*, "Visualization of magnetoencephalographic data using minimum current estimates," *Neuroimage,* vol. 10, pp. 173-180, Aug 1999.

[26] M. X. Huang, *et al.*, "Vector-based spatial-temporal minimum L1-norm solution for MEG," *Neuroimage,* vol. 31, pp. 1025-1037, Jul 1 2006.

[27] L. Ding and B. He, "Sparse source imaging in electroencephalography with accurate field modeling," *Human Brain Mapping,* vol. 29, pp. 1053-1067, Sep 2008.

[28] F. Luan, *et al.*, "A particle swarm optimization algorithm with novel expected fitness evaluation for robust optimization problems," *Ieee Transactions on Magnetics,* vol. 48, pp. 331-334, Feb 2012.

[29] F. Darvas, *et al.*, "Mapping human brain function with MEG and EEG: methods and validation," *Neuroimage,* vol. 23, pp. S289-S299, 2004.

[30] B. He, *et al.*, "Electrophysiological imaging of brain activity and connectivity—Challenges and opportunities," *Ieee Transactions on Biomedical Engineering,* vol. 58, pp. 1918-1931, Jul 2011.

[31] C. H. Im, *et al.*, "Anatomically constrained dipole adjustment (ANACONDA) for accurate MEG/EEG focal source localizations," *Physics in Medicine and Biology,* vol. 50, pp. 4931-4953, Oct 21 2005.

[32] A. Gramfort, *et al.*, "Tracking cortical activity from M/EEG using graph cuts with spatiotemporal constraints," *Neuroimage,* vol. 54, pp. 1930-1941, Feb 1 2011.

[33] A. Hillebrand and G. R. Barnes, "Practical constraints on estimation of source extent with MEG beamformers," *Neuroimage,* vol. 54, pp. 2732-2740, Feb 14 2011.

[34] F. Luan, *et al.*, "A comparison of regularization techniques for magnetoencephalography source reconstruction," *Ieee Transactions on Magnetics,* vol. 46, pp. 3209-3212, Aug 2010.

[35] F. Babiloni, *et al.*, "Multimodal integration of high-resolution EEG and functional magnetic resonance imaging data: a simulation study," *Neuroimage,* vol. 19, pp. 1-15, May 2003.

[36] F. Babiloni, *et al.*, "Multimodal integration of EEG and MEG data: A simulation study with variable signal-to-noise ratio and number of sensors," *Human Brain Mapping,* vol. 22, pp. 52-62, May 2004.

[37] H. Hallez, *et al.*, "Review on solving the forward problem in EEG source analysis," *Journal of Neuroengineering and Rehabilitation,* vol. 4, Nov 30 2007.

[38] G. Bonmassar, *et al.*, "Spatiotemporal brain imaging of visual-evoked activity using interleaved EEG and fMRI recordings," *Neuroimage,* vol. 13, pp. 1035-1043, Jun 2001.

[39] C. Lee, *et al.*, "Estimation of solution accuracy from leadfield matrix in magnetoencephalography," *Ieee Transactions on Magnetics,* vol. 43, pp. 1701-1704, Apr 2007.

[40] J. Schreiber, *et al.*, "A new method for choosing the regularization parameter in time-dependent inverse problems and its application to magnetocardiography," *Ieee Transactions on Magnetics,* vol. 40, pp. 1104-1107, Mar 2004.

[41] R. Bortel and P. Sovka, "Regularization techniques in realistic Laplacian computation," *Ieee Transactions on Biomedical Engineering,* vol. 54, pp. 1993-1999, Nov 2007.

[42] J. F. P. J. Abascal*, et al.*, "Comparison of methods for optimal choice of the regularization parameter for linear electrical impedance tomography of brain function," *Physiological Measurement,* vol. 29, pp. 1319-1334, Nov 2008.

[43] T. Correia*, et al.*, "Selection of regularization parameter for optical topography," *Journal of Biomedical Optics,* vol. 14, May-Jun 2009.

[44] S. Haufe*, et al.*, "Combining sparsity and rotational invariance in EEG/MEG source reconstruction," *Neuroimage,* vol. 42, pp. 726-738, Aug 15 2008.

[45] Y. Kim and P. A. Nelson, "Optimal regularisation for acoustic source reconstruction by inverse methods," *Journal of Sound and Vibration,* vol. 275, pp. 463-487, Aug 23 2004.

[46] H. G. Choi*, et al.*, "A threshold for the use of Tikhonov regularization in inverse force determination," *Applied Acoustics,* vol. 67, pp. 700-719, Jul 2006.

[47] H. G. Choi*, et al.*, "Comparison of methods for parameter selection in Tikhonov regularization with application to inverse force determination," *Journal of Sound and Vibration,* vol. 304, pp. 894-917, Jul 24 2007.

[48] G. H. Golub*, et al.*, "Generalized cross-validation as a method for choosing a good ridge parameter," *Technometrics,* vol. 21, pp. 215-223, 1979.

[49] P. C. Hansen, "Analysis of discrete ill-posed problems by means of the L-curve," *Siam Review,* vol. 34, pp. 561-580, Dec 1992.

[50] P. C. Hansen and D. P. Oleary, "The use of the L-curve in the regularization of discrete ill-posed problems," *Siam Journal on Scientific Computing,* vol. 14, pp. 1487-1503, Nov 1993.

[51] A. M. Dale and M. I. Sereno, "Improved localization of cortical activity by combining EEG and MEG with MRI cortical surface reconstruction - a linear approach," *Journal of Cognitive Neuroscience,* vol. 5, pp. 162-176, Spr 1993.

[52] K. Uutela*, et al.*, "Global optimization in the localization of neuromagnetic sources," *Ieee Transactions on Biomedical Engineering,* vol. 45, pp. 716-723, Jun 1998.

[53] M. A. Quraan*, et al.*, "Detection and localization of hippocampal activity using beamformers with MEG: a detailed investigation using simulations and empirical data," *Human Brain Mapping,* vol. 32, pp. 812-827, May 2011.

[54] K. O. An*, et al.*, "Improved magnetoencephalography source reconstruction considering anatomical connectivity of cortical sources," *Ieee Transactions on Magnetics,* vol. 42, pp. 1379-1382, Apr 2006.

[55] A. Moiseev*, et al.*, "Application of multi-source minimum variance beamformers for reconstruction of correlated neural activity," *Neuroimage,* vol. 58, pp. 481-496, Sep 15 2011.

[56] I. Kumihashi and K. Sekihara, "Array-gain constraint minimum-norm spatial filter with recursively updated gram matrix for biomagnetic source imaging," *Ieee Transactions on Biomedical Engineering,* vol. 57, pp. 1358-1365, Jun 2010.

[57] M. A. Quraan and D. Cheyne, "Reconstruction of correlated brain activity with adaptive spatial filters in MEG," *Neuroimage,* vol. 49, pp. 2387-2400, Feb 1 2010.

[58] J. M. Schoffelen and J. Gross, "Source connectivity analysis with MEG and EEG," *Human Brain Mapping,* vol. 30, pp. 1857-1865, Jun 2009.

[59] F. Luan*, et al.*, "Precise estimation of correlated bio-electromagnetic activities in deep source space," *Ieee Transactions on Magnetics,* vol. 48, pp. 339-342, Feb 2012.

[60] A. K. Liu, *et al.*, "Monte Carlo simulation studies of EEG and MEG localization accuracy," *Human Brain Mapping,* vol. 16, pp. 47-62, May 2002.

[61] C. H. Im, *et al.*, "Enhancing accuracy in magneto- and electroencephalography focal source localization," *Ieee Transactions on Magnetics,* vol. 42, pp. 1387-1390, Apr 2006.

[62] L. Ding, *et al.*, "Ictal source analysis: Localization and imaging of causal interactions in humans," *Neuroimage,* vol. 34, pp. 575-586, Jan 15 2007.

[63] H. B. Hui, *et al.*, "Identifying true cortical interactions in MEG using the nulling beamformer," *Neuroimage,* vol. 49, pp. 3161-3174, Feb 15 2010.

[64] A. K. Seth, "A MATLAB toolbox for Granger causal connectivity analysis," *Journal of Neuroscience Methods,* vol. 186, pp. 262-273, Feb 15 2010.

[65] G. Gomez-Herrero, *et al.*, "Measuring directional coupling between EEG sources," *Neuroimage,* vol. 43, pp. 497-508, Nov 15 2008.

[66] C. H. Im and H. J. Hwang, "EEG-based real-time dynamic neuroimaging," *Conference Proceedings IEEE Engineering in Medicine and Biology Society,* vol. 2009, pp. 5385-8, 2009.

[67] M. Diwakar, *et al.*, "Dual-core beamformer for obtaining highly correlated neuronal networks in MEG," *Neuroimage,* vol. 54, pp. 253-263, Jan 1 2011.

[68] F. Luan, *et al.*, "Comparison and improvement of inverse techniques for MEG source connectivity network reconstruction," *Ieee Transactions on Magnetics,* vol. 48, pp. 343-346, Feb 2012.

[69] A. Dossevi, *et al.*, "Multivariate reconstruction of functional networks from cortical sources dynamics in MEG/EEG," *Ieee Transactions on Biomedical Engineering,* vol. 55, pp. 2074-2086, Aug 2008.

[70] J. M. Schoffelen and J. Gross, "Improving the interpretability of all-to-all pairwise source connectivity analysis in MEG with

nonhomogeneous smoothing," *Human Brain Mapping,* vol. 32, pp. 426-437, Mar 2011.

[71] B. L. P. Cheung*, et al.*, "Estimation of cortical connectivity from EEG using state-space models," *Ieee Transactions on Biomedical Engineering,* vol. 57, pp. 2122-2134, Sep 2010.

[72] A. Hillebrand*, et al.*, "Frequency-dependent functional connectivity within resting-state networks: An atlas-based MEG beamformer solution," *Neuroimage,* vol. 59, pp. 3909-3921, Feb 15 2012.

[73] B. He*, et al.*, "eConnectome: A MATLAB toolbox for mapping and imaging of brain functional connectivity," *Journal of Neuroscience Methods,* vol. 195, pp. 261-269, Feb 15 2011.

[74] K. Sekihara*, et al.*, "Localization bias and spatial resolution of adaptive and non-adaptive spatial filters for MEG source reconstruction," *Neuroimage,* vol. 25, pp. 1056-1067, May 1 2005.

[75] K. O. An*, et al.*, "Estimation of brain electrical sources using multilevel source space model," *Ieee Transactions on Magnetics,* vol. 43, pp. 1697-1700, Apr 2007.

[76] D. Marinazzo*, et al.*, "Nonlinear connectivity by Granger causality," *Neuroimage,* vol. 58, pp. 330-338, Sep 15 2011.

[77] D. W. Gow Jr.*, et al.*, "Lexical influences on speech perception: A Granger causality analysis of MEG and EEG source estimates," *Neuroimage,* vol. 43, pp. 614-623, Nov 15 2008.

[78] H. Gao*, et al.*, "Robust principal component analysis-based four-dimensional computed tomography," *Physics in Medicine and Biology,* vol. 56, pp. 3181-3198, Jun 7 2011.

[79] F. Luan*, et al.*, "Measurement of bio-electromagnetic source signal via subspace decomposition imaging," *Electronics Letters,* vol. 48, pp. 364-U94, Mar 29 2012.

[80] E. J. Candes*, et al.*, "Robust principal component analysis?," *Journal of the Acm,* vol. 58, May 2011.

[81] Z. Lin, *et al.*, "The augmented Lagrange multiplier method for exact recovery of corrupted low-rank matrices," University of Illinois at Urbana-Champaign, technical report, UILU-ENG-09-2215, 2009.

[82] X. H. Ding, *et al.*, "Bayesian robust principal component analysis," *Ieee Transactions on Image Processing,* vol. 20, pp. 3419-3430, Dec 2011.

[83] A. Beck and M. Teboulle, "A Fast Iterative Shrinkage-Thresholding Algorithm for Linear Inverse Problems," *Siam Journal on Imaging Sciences,* vol. 2, pp. 183-202, 2009.

[84] V. Chandrasekaran, *et al.*, "Rank-sparsity incoherence for matrix decomposition," *Siam Journal on Optimization,* vol. 21, pp. 572-596, 2011.

[85] L. Tyvaert, *et al.*, "Noninvasive dynamic imaging of seizures in epileptic patients," *Human Brain Mapping,* vol. 30, pp. 3993-4011, Dec 2009.

[86] F. Tadel, *et al.*, "Brainstorm: a user-friendly application for MEG/EEG analysis," *Computational Intelligence and Neuroscience,* vol. 2011, p. 879716, 2011.

[87] P. Zwolinski, *et al.*, "Open database of epileptic EEG with MRI and postoperational assessment of foci-A real world verification for the EEG inverse solutions," *Neuroinformatics,* vol. 8, pp. 285-299, Dec 2010.

[88] G. Wang, *et al.*, "Interictal spike analysis of high-density EEG in patients with partial epilepsy," *Clinical Neurophysiology,* vol. 122, pp. 1098-1105, Jun 2011.

[89] L. Ding, *et al.*, "3D source localization of interictal spikes in epilepsy patients with MRI lesions," *Physics in Medicine and Biology,* vol. 51, pp. 4047-4062, Aug 21 2006.

[90] L. Ding, *et al.*, "EEG source imaging: Correlating source locations and extents with electrocorticography and surgical resections in epilepsy patients," *Journal of Clinical Neurophysiology,* vol. 24, pp. 130-136, Apr 2007.

[91] L. Yang, *et al.*, "Dynamic imaging of ictal oscillations using non-invasive high-resolution EEG," *Neuroimage,* vol. 56, pp. 1908-1917, Jun 15 2011.

[92] G. Scheler, *et al.*, "Spatial relationship of source localizations in patients with focal epilepsy: Comparison of MEG and EEG with a three spherical shells and a boundary element volume conductor model," *Human Brain Mapping,* vol. 28, pp. 315-322, Apr 2007.

[93] H. Shiraishi, "Source localization in magnetoencephalography to identify epileptogenic foci," *Brain & Development,* vol. 33, pp. 276-281, Mar 2011.

[94] R. Bouet, *et al.*, "Towards source volume estimation of interictal spikes in focal epilepsy using magnetoencephalography," *Neuroimage,* vol. 59, pp. 3955-3966, Feb 15 2012.

[95] C. H. Im, *et al.*, "Assessment criteria for MEG/EEG cortical patch tests," *Physics in Medicine and Biology,* vol. 48, pp. 2561-2573, Aug 7 2003.

[96] J. H. Cho, *et al.*, "Evaluation of algorithms for intracranial EEG (iEEG) source imaging of extended sources: feasibility of using iEEG source imaging for localizing epileptogenic zones in secondary generalized epilepsy," *Brain Topography,* vol. 24, pp. 91-104, Jun 2011.

[97] C. H. Im, *et al.*, "Reconstruction of continuous and focalized brain functional source images from electroencephalography," *Ieee Transactions on Magnetics,* vol. 43, pp. 1709-1712, Apr 2007.

[98] J. M. Zumer, *et al.*, "A probabilistic algorithm integrating source localization and noise suppression for MEG and EEG data," *Neuroimage,* vol. 37, pp. 102-115, Aug 1 2007.

[99] G. Crevecoeur, *et al.*, "Influence of noise on EEG source analysis using space mapping techniques," *International Journal of Applied Electromagnetics and Mechanics,* vol. 25, pp. 383-387, 2007.

[100] G. Van Hoey, *et al.*, "Influence of measurement noise and electrode mislocalisation on EEG dipole-source localisation," *Medical &*

Biological Engineering & Computing, vol. 38, pp. 287-296, May 2000.

초록

뇌자도는 뇌 안쪽에 존재하는 뉴런의 조합에 의해 생성되는 약한 전자기장을 비침습적으로 측정할 수 있는 생물의학적인 기법이다. 신경전자기신호원 해석의 주요 목표는 외부에서 측정된 전자기장을 이용해서 신호원 활동의 기능적 정보를 제공하기 위해 특정시점에서의 신호원 분포와 위치를 파악하는 것이다. 이 문제는 부가적인 제안조건이 주어지지 않으면 유일한 신경전자기신호원을 복원할 수 없는 역문제의 일종이다. 본 논문에서는 정확하게 신호원을 복원할 수 있는 다양한 제안조건과 기법들을 소개하고 새로운 기법들을 제안하였다.

잡음이 수반된 측정치를 이용해 신호원을 복원하는 경우 최적의 정규변수를 추정해야 하는데 이 과정에서 널리 사용되고 있는 일반교차평가법(GCV)과 L-curve 방법을 비교, 분석하였다. 일반교차평가법은 센서잡음이 높은 경우에 정규변수를 정확히 추정하였고 L-curve 방법은 신호원잡음이 높은 경우에 GCV 보다 정규변수를 정확히 추정한다는 결과를 얻었다.

뇌 안쪽에 위치한 연결성이 있는 신경전자기신호원 활동을 정확히 복원하기 위해 개선된 역문제기법을 제안하였다. 신호원과 측정센서 사이의 민감유사도를 이용한 새로운 가중치 행렬 설계법을 제안했으며 이는 연결된 깊은 신호원의 특성을 복원하는데 효과적이었다. 시뮬레이션 결과 제안된 비법은 기존 방법보다 신호원 추정에 구체적인 정보를 제공했으며 복원정확도를 높일 수 있었다.

최근 신경전자기신호원의 연결성 분석에 대한 연구가 활발히 진행되고 있다. 본 논문에서는 신호원의 연결성을 복원하는 기법에 대한 비교연구를 진행하였다. 선형추정법은 외부잡음에 직접적인 영향을 받으며 공간필터법은 잡음에 민감하지 않은 특성을 가지는데 본 연구에서는 신호원의 연결성을 정밀히 추정하기 위해 공간필터법을 발전시킨 새로운 기법을 제안했다. 시뮬레이션 결과를 통해 새로운 기법이 기존 방법보다 평균 정확도를 향상시키고 오차의 분산을 줄일 수 있다는 것을 확인하였다.

마지막으로 본 논문에서는 신경전자기신호원의 다양한 시공간적 변화를 추정할 수 있는 부분공간분해영상법(SDI)을 제안하였다. 신호원이 순간적인 변화를 가지는 성분과 안정적인 성분이 동시에 존재하는 경우 공간분해법을 통해 각각 추정하여 신경신호원의 분포 및 시간에 따른 변화를 복원할 수 있었다. 측정된 뇌자도 데이터의 잡음성분을 제거하거나 이를 고려해 신경전자기신호원을 복원하기 위해 부분공간분해영상법(SDI)을 이용했으며 신호원 복원 결과를 현저하게 향상시킬 수 있었다.

키워드: 전자기적 뇌영상, 뇌자도(MEG), 신경전자기 역문제, 신호원 영상, 부분공간분해영상(SDI)

학번: 2008-31105

Acknowledgment

I would like to thank all of those who have supported me through my research. In particular, I would like to express my sincere sense of gratitude to my supervisor, Professor Hyun-Kyo Jung, Department of Electrical Engineering and Computer Science, Seoul National University, for his continuous support and guidance not only in my studies but also in all the times which I had faced during my stay in Korea.

I am extremely thankful to my mates and my seniors who made my stay in Korea an unforgettable experience. All my lab members helped me out throughout all discussions and seminars. I will never forget this wonderful group of people and will surely cherish the great memories that I shared with them for the rest of my life. I wish all the best to the members of Electromechanics Lab.

This thesis would never have been completed without the support of my family. I would like to thank my wife for her love, support and encouragement in last several years. Last but not least, I would deeply grateful to my parents and brother for their greatest and selfless love and support.

Feng Luan